



An analytic model for the collisional transport and poloidal asymmetry distribution of impurities in tokamak plasmas

Patrick Maget, Pierre Manas, Judith Frank, Timothée Nicolas, Olivier Agullo, Xavier Garbet

► To cite this version:

Patrick Maget, Pierre Manas, Judith Frank, Timothée Nicolas, Olivier Agullo, et al.. An analytic model for the collisional transport and poloidal asymmetry distribution of impurities in tokamak plasmas. Plasma Physics and Controlled Fusion, 2020, 62, pp.105001. 10.1088/1361-6587/aba7f9 . cea-02572297v2

HAL Id: cea-02572297

<https://cea.hal.science/cea-02572297v2>

Submitted on 24 Aug 2020

HAL is a multi-disciplinary open access archive for the deposit and dissemination of scientific research documents, whether they are published or not. The documents may come from teaching and research institutions in France or abroad, or from public or private research centers.

L'archive ouverte pluridisciplinaire **HAL**, est destinée au dépôt et à la diffusion de documents scientifiques de niveau recherche, publiés ou non, émanant des établissements d'enseignement et de recherche français ou étrangers, des laboratoires publics ou privés.

An analytic model for the collisional transport and poloidal asymmetry distribution of impurities in tokamak plasmas

Patrick Maget, Pierre Manas, Judith Frank¹, Timothée Nicolas², Olivier Agullo¹, Xavier Garbet

CEA, IRFM, F-13108 Saint Paul-lez-Durance, France.

¹ Aix-Marseille Université, CNRS, PIIM UMR 7345, 13397 Marseille Cedex 20, France.

² Centre de Physique Théorique, CNRS, Ecole Polytechnique, Institut Polytechnique de Paris, Route de Saclay, 91128 PALAISEAU

E-mail: patrick.maget@cea.fr

Abstract. The coupling between the poloidal distribution and the collisional flux of impurities can be exploited to derive a simplified analytical model covering toroidal rotation and electrostatic potential asymmetry effects, valid in the Pfirsch-Schlüter regime. This model is compared with earlier works and with the drift-kinetic code NEO, which includes the full Fokker-Planck collision operator. The low computational cost of the model, compared to NEO, is particularly adapted for fast integrated simulation purposes.

1. Introduction

The transport of impurity ions (i.e. other than Deuterium and Tritium) represents a key issue in magnetic fusion research, mainly because of the radiative losses that they can induce in the plasma core. Metallic walls surrounding the plasma constitute a source of heavy and highly radiative ions that are of particular concern. Both collisional and turbulent processes impact impurity transport, and although in many cases turbulent transport is dominant [1, 2, 3], there is experimental evidence that collisional transport can compete and even overcome it in the plasma core where turbulence is reduced [4], or when it is largely reduced by a transport barrier [5, 6, 7, 8], in presence of large toroidal rotation [9, 10, 11, 12, 13, 14] or when using Ion Cyclotron Resonance Heating (ICRH) [15, 16, 17, 18, 14, 19, 20, 21]. These situations are not unusual in a tokamak, and often decide on the robustness of a scenario [22, 23, 24, 25].

The collisional impurity flux is composed of a classical part, independent of the poloidal variation of the magnetic field amplitude, and of a neoclassical part that is due to this poloidal variation. In the Pfirsch-Schlüter regime that is considered here, this neoclassical component is usually larger than the classical one, by a factor $2q^2$ (with

q the safety factor), but it is also strongly dependent on the poloidal distribution of the impurity [26, 27, 28]. The relation between the neoclassical flux and the poloidal asymmetry of the impurity can be formulated in a geometrical representation [29]. In this representation, the horizontal and vertical poloidal asymmetries are positioned on a circle whose characteristics depends on the plasma equilibrium, and the actual position on the circle is given by an angle depending on the collision frequency of the impurity with the main ions. The impurity flux derives directly from the resulting poloidal asymmetry, and for a given impurity profile, it can be sufficiently reduced by this asymmetry to become lower than the classical flux [26]. But the poloidal asymmetry changes as the impurity profile evolves to steady-state. This results from the fact that the impurity gradient is taken into account in the parallel force balance, thus coupling the poloidal distribution to the radial profile of the impurity. This coupling falls out of the conventional ordering of neoclassical theory [30], and generates a nonlinear dependence of the flux on the impurity gradient. In the simplest case (no toroidal rotation, poloidally symmetric electrostatic potential), the steady state impurity distribution has no asymmetry, so that the impurity peaking would be identical to the neoclassical prediction without poloidal asymmetry [29].

In the present work, we extend our analytic model to describe finite toroidal rotation (section 2), and we consider in section 3 three academic applications of interest for present fusion plasma experiments: the case of a "natural" plasma (no toroidal rotation, no ICRH heating), where we discuss the implication of a residual asymmetry of the electrostatic potential; the case of pure toroidal rotation; and the case of plasma heating at the Ion Cyclotron Resonance Frequency (ICRF) with the Hydrogen minority heating scheme. As mentioned above, the two last situations are well known to be prone to increase collisional transport at a level comparable or even above the turbulent one: centrifugal forces by pushing heavy impurities on the Low Field Side (LFS) of the torus, and ICRF heating by pushing them on the High Field Side (HFS) or LFS depending on the cyclotron resonance position [31], generate strong poloidal asymmetries that greatly enhance their neoclassical transport and can lead to deleterious accumulation in the plasma core [14]. Because of the strong link between the impurity gradient, the poloidal asymmetry and the flux, the impurity distribution, diffusion and pinch velocity vary during the evolution to steady state, invalidating some features of the flat profile situation, as exemplified by the "natural" case where the final impurity peaking loses any potential reduction. We compare our model with the drift-kinetic code NEO [32, 33, 34] for the three cases mentioned above, at the impurity gradient where the neoclassical flux cancels. This comparison is of particular interest since it allows evaluating the impact of breaking the standard neoclassical ordering that is used in NEO. The main results are summarized in section 4.

2. Collisional impurity flux and poloidal asymmetry

The collisional impurity flux can be expressed as the sum of a neoclassical and a classical parts. The neoclassical component is generally considered as dominant, since in the absence of poloidal asymmetries it exceeds the classical part by a factor $2q^2$ in the Pfirsch-Schlüter regime. But while the classical part is weakly affected by the poloidal distribution of the impurity, the neoclassical part can be drastically reduced and can become subdominant, in particular for highly charged species [26]. In this section, we express these two components of the flux in the general case together with the poloidal asymmetry constraint, and then we derive the analytic model in the large aspect ratio limit.

2.1. General case

In the Pfirsch-Schlüter regime, the neoclassical flux of an impurity species "a" in presence of toroidal rotation can be expressed as (see Appendix A):

$$\begin{aligned} \langle \Gamma_a^{neo} \cdot \nabla \psi \rangle = & m_a \nu_a \langle n_a \rangle \frac{F^2 T_a}{e_a^2 \langle B^2 \rangle} \left[\left(\frac{1}{\langle b^2/n \rangle} - \left\langle \frac{n}{b^2} \right\rangle \right) \mathcal{G}_\psi + \left(\frac{\langle b^2/N \rangle}{\langle b^2/n \rangle} - \left\langle \frac{n}{N} \right\rangle \right) \mathcal{U}_\psi \right. \\ & \left. + \frac{m_a \Omega^2}{2T_a} \left(1 - \frac{m_i e_a}{m_a e_i} \right) \left(\left\langle \frac{n \partial_\psi R^2}{b^2} \right\rangle - \frac{\langle \partial_\psi R^2 \rangle}{\langle b^2/n \rangle} \right) \right] \end{aligned} \quad (1)$$

where the equilibrium magnetic field is parametrized as $\mathbf{B} = F \nabla \varphi + \nabla \varphi \times \nabla \psi$ with φ the toroidal angle and ψ the poloidal magnetic flux. We note m_a the impurity mass, n_a its density, T_a its temperature and e_a its electric charge, ν_a the impurity-ion collision frequency, Ω the toroidal angular frequency, R is the major radius and the label "i" refers to the main ion species. In addition to toroidal rotation, the drive for the impurity flux is the impurity and main ion density and temperature gradients, that are contained in \mathcal{G}_ψ and \mathcal{U}_ψ as follows:

$$\mathcal{G}_\psi \equiv \partial_\psi \ln p_a - \frac{T_i}{T_a} \frac{e_a}{e_i} \partial_\psi \ln p_i + C_0^a \frac{T_i}{T_a} \frac{e_a}{e_i} \partial_\psi \ln T_i \quad (2)$$

$$\mathcal{U}_\psi \equiv u(\psi) \frac{\langle B^2 \rangle}{F} \frac{e_a}{T_a} \quad (3)$$

where $u(\psi)$ is a term related to thermal screening (see eq. (45)), and $C_0^a \approx 1.5$ for heavy impurities (see also Appendix A).

This neoclassical flux is complemented by a classical flux that can be expressed, in the limit where $\nabla \psi \cdot \nabla \theta \approx 0$, as:

$$\begin{aligned} \langle \Gamma_a^{cl} \cdot \nabla \psi \rangle \approx & - \frac{m_a \nu_a \langle n_a \rangle F^2 T_a}{e_a^2 \langle B^2 \rangle} \left[\left(\frac{\langle B^2 \rangle}{F^2} \langle n R^2 \rangle - \left\langle \frac{n}{b^2} \right\rangle \right) \mathcal{G}_\psi \right. \\ & \left. - \frac{m_a \Omega^2}{2T_a} \left(1 - \frac{m_i e_a}{m_a e_i} \right) \left(\frac{\langle B^2 \rangle}{F^2} \langle n R^2 \partial_\psi R^2 \rangle - \left\langle \frac{n \partial_\psi R^2}{b^2} \right\rangle \right) \right] \end{aligned} \quad (4)$$

that can be further approximated as (see Appendix B):

$$\langle \Gamma_a^{cl} \cdot \nabla \psi \rangle \approx - \frac{m_a \nu_a \langle n_a \rangle F^2 T_a}{e_a^2 \langle B^2 \rangle} \left(\frac{\epsilon}{q} \right)^2 \left[\left\langle \frac{n}{b^2} \right\rangle \mathcal{G}_\psi - \frac{m_a \Omega^2}{2T_a} \left(1 - \frac{m_i e_a}{m_a e_i} \right) \left\langle \frac{n \partial_\psi R^2}{b^2} \right\rangle \right] \quad (5)$$

with $\epsilon = r/R_0$ and R_0 the major radius of the magnetic axis. The poloidal variation of the magnetic field, and of the impurity and main ion densities are contained respectively in b , n and N :

$$b^2 = B^2 / \langle B^2 \rangle \quad (6)$$

$$n = n_a / \langle n_a \rangle \quad (7)$$

$$N = n_i / \langle n_i \rangle \quad (8)$$

The neoclassical impurity flux is primarily driven by the poloidal variation of the equilibrium magnetic field, but the poloidal distribution of the impurity density also responds to this inhomogeneity and can strongly alter in return the amplitude of the flux. The poloidal distribution of the impurity can be determined from the parallel force balance (see Appendix A.3):

$$\begin{aligned} \partial_\theta \ln n_a + \frac{e_a}{T_a} \partial_\theta \phi - \frac{m_a \Omega^2}{2T_a} \partial_\theta R^2 = \mathcal{A}_\psi \left\{ \left(1 - \frac{b^2/n}{\langle b^2/n \rangle} \right) \mathcal{G}_\psi + \left(\frac{b^2}{N} - \left\langle \frac{b^2}{N} \right\rangle \frac{b^2/n}{\langle b^2/n \rangle} \right) \mathcal{U}_\psi \right. \\ \left. + \frac{m_a \Omega^2}{2T_a} \left(1 - \frac{m_i e_a}{m_a e_i} \right) \left(\frac{b^2/n}{\langle b^2/n \rangle} \langle \partial_\psi R^2 \rangle - \partial_\psi R^2 \right) \right\} \quad (9) \end{aligned}$$

with $\mathcal{A}_\psi = JF m_a \nu_a / e_a$, and J is the Jacobian of the co-ordinate system (ψ, θ, φ) . It depends therefore on toroidal rotation and on the poloidal asymmetry of the electrostatic potential, but also on the friction force with the main ions.

2.2. Large aspect ratio limit

2.2.1. Radial flux The neoclassical impurity flux (equation 1) and the poloidal asymmetries (equation 9) can be both related in a simple way in the large aspect ratio limit, when retaining only the sine and cosine components of the poloidal Fourier decomposition:

$$b = 1 - \epsilon \cos \theta \quad (10)$$

$$n = 1 + \delta \cos \theta + \Delta \sin \theta \quad (11)$$

$$N = 1 + \delta_N \cos \theta + \Delta_N \sin \theta \quad (12)$$

$$\frac{e\phi}{T_e} = \frac{e \langle \phi \rangle}{T_e} + \delta_\phi \cos \theta + \Delta_\phi \sin \theta \quad (13)$$

In the following we note $(\delta_\phi^a, \Delta_\phi^a) = Z_a(T_e/T_a)(\delta_\phi, \Delta_\phi)$. We then obtain for the neoclassical impurity flux (see Appendix B):

$$\begin{aligned} \langle \Gamma_a^{neo} \cdot \nabla r \rangle \approx - \langle n_a \rangle \frac{D_{PS}^a}{R_0} \left[\left(1 + \frac{\delta}{\epsilon} + \frac{\delta^2 + \Delta^2}{4\epsilon^2} \right) \mathcal{G} \right. \\ \left. + \frac{1}{2} \left(\frac{\delta - \delta_N}{\epsilon} + \frac{\delta^2 + \Delta^2 - \delta\delta_N - \Delta\Delta_N}{2\epsilon^2} \right) \mathcal{U} \right. \\ \left. - \frac{\delta_M}{2\epsilon^2} \left(1 - \frac{m_i e_a}{m_a e_i} \right) \left(1 + \frac{\delta}{2\epsilon} \right) \right] \quad (14) \end{aligned}$$

with $D_{PS}^a \equiv 2q^2 m_a \nu_a T_a / (e_a^2 \langle B^2 \rangle)$, $q = rB_0 / \partial_r \psi$ with B_0 the magnetic field at the magnetic axis, $\delta_M = \epsilon m_a (R_0 \Omega)^2 / T_a$, $\mathcal{G} = (rR_0 B_0 / q) \mathcal{G}_\psi$ and $\mathcal{U} = (rR_0 B_0 / q) \mathcal{U}_\psi$. Note that we have also $\delta_M = 2\epsilon(m_a/m_i)(T_i/T_a)M_i^2$ with M_i the ion Mach number.

The classical heat flux can be derived in a similar way from equation (5):

$$\langle \Gamma_a^{cl} \cdot \nabla r \rangle \approx - \langle n_a \rangle \frac{D_{PS}^a}{2q^2 R_0} \left[(1 + \epsilon \delta + 2\epsilon^2) \mathcal{G} - \frac{3\delta_M}{2} \left(1 - \frac{m_i e_a}{m_a e_i} \right) \left(1 + \frac{\delta}{3\epsilon} \right) \right] \quad (15)$$

This flux is typically lower than the neoclassical one by a factor $\sim 2q^2$ when poloidal asymmetry is neglected. But for highly charged impurities, the neoclassical flux can be strongly reduced by poloidal asymmetries and the classical flux can then represent a larger contribution [26, 29]. The classical flux is also less sensitive to the poloidal impurity distribution, except for the toroidal rotation term.

2.2.2. Poloidal asymmetry The equation (9) containing the constraints on the poloidal asymmetry parameters can be expressed as a system of equations relating the sine and cosine components:

$$\delta + \delta_\phi^a - \delta_M = - \mathcal{A} [\Delta \mathcal{G} + (\Delta - \Delta_N) \mathcal{U} - \mathcal{R} \delta_M \epsilon \Delta] \quad (16)$$

$$\Delta + \Delta_\phi^a = \mathcal{A} [(2\epsilon + \delta) \mathcal{G} + (\delta - \delta_N) \mathcal{U} - 2\mathcal{R} \delta_M] \quad (17)$$

with $\mathcal{A} = q/(rR_0 B_0) \mathcal{A}_\psi$ and

$$\mathcal{R} = \frac{1}{2\epsilon} \left(1 - \frac{m_i e_a}{m_a e_i} \right) \quad (18)$$

The parameter \mathcal{A} measures the collisional friction, \mathcal{G} the radial gradients, \mathcal{U} the ion temperature gradient, and \mathcal{R} the weight of toroidal rotation. These relations evidence the tilting of the poloidal asymmetry of the impurity due to parallel friction forces that couple the horizontal and vertical components (δ , Δ) [26, 12, 35].

The poloidal asymmetry parameters for the density of the impurity (δ , Δ) can be related by eliminating the collisionality parameter \mathcal{A} in the system of equations (17) and (16), as was done in [29]. We introduce the following notations:

$$C_\delta^0 = - \epsilon / (1 + \mathcal{U}/\mathcal{G}) \quad (19)$$

$$\mathcal{F} = C_\delta^0 \left(1 - \frac{\delta_N \mathcal{U}}{2\epsilon \mathcal{G}} - \frac{\delta_M \mathcal{R}}{\epsilon \mathcal{G}} \right) \quad (20)$$

$$\mathcal{H} = 1 + \delta_M C_\delta^0 \frac{\mathcal{R}}{\mathcal{G}} \quad (21)$$

$$\mathcal{Q} = C_\delta^0 \frac{\Delta_N \mathcal{U}}{\epsilon \mathcal{G}} \quad (22)$$

so that equations (16) and (17) can be expressed as:

$$\delta + \delta_\phi^a - \delta_M = \frac{\mathcal{A} \mathcal{G} \epsilon}{C_\delta^0} [\Delta \mathcal{H} + \mathcal{Q}] \quad (23)$$

$$\Delta + \Delta_\phi^a = - \frac{\mathcal{A} \mathcal{G} \epsilon}{C_\delta^0} [\delta - 2\mathcal{F}] \quad (24)$$

This leads to

$$(\delta - C_\delta)^2 + \mathcal{H} (\Delta - C_\Delta)^2 = R_\Delta^2 \quad (25)$$

with

$$C_\delta = \mathcal{F} - \frac{\delta_\phi^a - \delta_M}{2} \quad (26)$$

$$C_\Delta = -\frac{1}{2} \left(\frac{\mathcal{Q}}{\mathcal{H}} + \Delta_\phi^a \right) \quad (27)$$

$$R_\Delta^2 = \left(\mathcal{F} + \frac{\delta_\phi^a - \delta_M}{2} \right)^2 + \frac{\mathcal{H}}{4} \left(\Delta_\phi^a - \frac{\mathcal{Q}}{\mathcal{H}} \right)^2 \quad (28)$$

The curve (δ, Δ) defined in equation (25) is an ellipsis when toroidal rotation is present ($\mathcal{H} \neq 1$) and it can be parametrized as:

$$\delta = C_\delta + R_\Delta \cos \alpha \quad (29)$$

$$\Delta = C_\Delta + R_\Delta (\mathcal{H})^{-1/2} \sin \alpha \quad (30)$$

The collisional angle α can then be derived and we obtain:

$$\begin{aligned} \cos \alpha &= \frac{R_\Delta C_\delta^0}{\mathcal{D}} \left\{ \left[\left(\frac{\mathcal{A}\mathcal{G}\epsilon}{C_\delta^0} \right)^2 \mathcal{H} - 1 \right] \left(\frac{\mathcal{F}}{C_\delta^0} + \frac{\delta_\phi^a - \delta_M}{2C_\delta^0} \right) \right. \\ &\quad \left. + \frac{\mathcal{A}\mathcal{G}\epsilon}{C_\delta^0} \left[\frac{\Delta_N \mathcal{U}}{2\epsilon \mathcal{G}} - \mathcal{H} \frac{\Delta_\phi^a}{2C_\delta^0} \right] \right\} \end{aligned} \quad (31)$$

$$\begin{aligned} \sin \alpha &= \frac{R_\Delta C_\delta^0}{\mathcal{D}} \mathcal{H}^{1/2} \left\{ \left[\left(\frac{\mathcal{A}\mathcal{G}\epsilon}{C_\delta^0} \right)^2 \mathcal{H} - 1 \right] \left(\frac{\Delta_\phi^a}{2C_\delta^0} - \frac{\Delta_N}{2\epsilon} \frac{\mathcal{U}}{\mathcal{G}\mathcal{H}} \right) \right. \\ &\quad \left. + 2 \frac{\mathcal{A}\mathcal{G}\epsilon}{C_\delta^0} \left(\frac{\mathcal{F}}{C_\delta^0} + \frac{\delta_\phi^a - \delta_M}{2C_\delta^0} \right) \right\} \end{aligned} \quad (32)$$

with $\mathcal{D} = R_\Delta^2 + \mathcal{H} (\mathcal{A}\mathcal{G}\epsilon)^2 (R_\Delta/C_\delta^0)^2$. The system of equations (26), (27), (28), (29), (30), (31), (32) fully determines the asymmetry of the impurity density as a function of its collisional friction with the main ions (\mathcal{A}), of the main ion and impurity gradients (\mathcal{G} and \mathcal{U}), toroidal rotation (\mathcal{H}) and of the asymmetries of the main ion density (δ_N , Δ_N) and electrostatic potential (δ_ϕ , Δ_ϕ). This asymmetry gives in return the impurity flux expressed in equations (14) and (15). From these equations we can extract the total (classical plus neoclassical) diffusion coefficient D_a and pinch velocity V_a :

$$\langle \Gamma_a^{tot} \cdot \nabla r \rangle = -D_a \partial_r \langle n_a \rangle + \langle n_a \rangle V_a \quad (33)$$

$$D_a = D_a^{neo} + D_a^{cl} \quad (34)$$

$$V_a = V_a^{neo} + V_a^{cl} \quad (35)$$

where:

$$D_a^{neo} = D_{PS}^a \left(1 + \frac{\delta}{\epsilon} + \frac{\delta^2 + \Delta^2}{4\epsilon^2} \right) \quad (36)$$

$$D_a^{cl} = \frac{D_{PS}^a}{2q^2} (1 + \epsilon\delta + 2\epsilon^2) \quad (37)$$

$$\begin{aligned} V_a^{neo} &= -\frac{D_{PS}^a}{R_0} \left[\left(1 + \frac{\delta}{\epsilon} + \frac{\delta^2 + \Delta^2}{4\epsilon^2} \right) \mathcal{G}^V \right. \\ &\quad \left. + \frac{1}{2} \left(\frac{\delta - \delta_N}{\epsilon} + \frac{\delta^2 + \Delta^2 - \delta\delta_N - \Delta\Delta_N}{2\epsilon^2} \right) \mathcal{U} \right] \end{aligned}$$

$$-\frac{\delta_M}{2\epsilon^2} \left(1 - \frac{m_i e_a}{m_a e_i}\right) \left(1 + \frac{\delta}{2\epsilon}\right) \quad (38)$$

$$V_a^{cl} = -\frac{D_{PS}^a}{2q^2 R_0} \left[(1 + \epsilon\delta + 2\epsilon^2) \mathcal{G}^V - \frac{3\delta_M}{2} \left(1 - \frac{m_i e_a}{m_a e_i}\right) \left(1 + \frac{\delta}{3\epsilon}\right) \right] \quad (39)$$

$$\text{with } \mathcal{G}^V \equiv R_0 \left(\partial_r \ln T_a - \frac{T_i e_a}{T_a e_i} \partial_r \ln p_i + C_0^a \frac{T_i e_a}{T_a e_i} \partial_r \ln T_i \right).$$

3. Applications

In this section, we illustrate the potential applications of the analytic model by considering first the "natural" case, and then two situations where the neoclassical transport of impurities can compete with turbulent processes: toroidal rotation and Ion Cyclotron Resonance Heating, in the core region. For this, we need to determine the asymmetries of the main ion density and electrostatic potential. We consider a Boltzmann distribution of both electrons and main ions, and this leads to an electrostatic potential that has a horizontal asymmetry driven by the anisotropic temperature of the minority ions and by toroidal rotation [17, 16]:

$$\delta\phi = \frac{\epsilon}{1 + Z_i T_e / T_i} \left[f_H \left(\frac{T_\perp}{T_\parallel} - 1 \right) \frac{b_C}{b_C + \frac{T_\perp}{T_\parallel} (1 - b_C)} + m_i \frac{(R_0 \Omega)^2}{T_i} \right] \quad (40)$$

with f_H the Hydrogen minority fraction, $b_C = B^{res}/B_0$ and B^{res} the magnetic field where the ICRH frequency matches the fundamental cyclotron resonance of the minority ion.

In addition to this horizontal asymmetry driven by rotation and ICRF heating, a small residual asymmetry of the electrostatic potential is spontaneously driven by collisions, and this residual is particularly important in the "natural" case. This asymmetry is essentially vertical [36], as found with PIC simulations [37] and with NEO [32]. An analytic derivation by Wong et al [38] will be used here. It exhibits a sharp discontinuity at $\theta = \pm\pi$ that is expected to be smoothed by collisions, and a simplified expression for the natural Δ_ϕ can be derived from this work:

$$\Delta_\phi^{nat} \approx \frac{C^{nat.}}{Z_i + T_e/T_i} \frac{q^2 x}{\epsilon^{5/2}} \frac{\partial_x \ln T_i}{\tau_{ii} \Omega_i} \quad (41)$$

with $C^{nat} \approx -0.165$ and $\Omega_i \equiv e_i B_0 / m_i$.

For the poloidal variation of the main ion density, we get from the parallel force balance without collisions (equation 9):

$$n_i = \langle n_i \rangle \exp \left(-\frac{e_i \phi}{T_i} + \frac{m_i \Omega^2}{2T_i} (R^2 - \langle R^2 \rangle) \right) \quad (42)$$

which gives :

$$\delta_N = -Z_i \frac{T_e}{T_i} \delta\phi + \frac{\epsilon m_i (R_0 \Omega)^2}{T_i} \quad (43)$$

$$\Delta_N = -Z_i \frac{T_e}{T_i} \Delta_\phi \quad (44)$$

The parameter \mathcal{U} can be expressed in a simple way after considering the fact that neoclassical friction constrains the poloidal flow. This gives (see [29]):

$$u(\psi) \approx - \frac{C_0^a + k_i T_i q}{\langle B^2 \rangle} \frac{q}{e_i \epsilon} \partial_r \ln T_i \quad (45)$$

with k_i a neoclassical friction coefficient that tends asymptotically to -1.17 in the banana regime. This coefficient as well as the collision frequency ν_a are computed following the model described in Kessel [39]. Note that this model, as the NCLASS model [40], is inaccurate in the high collisionality regime where ion-electron coupling becomes important, i.e. typically in the edge region [41].

We consider geometrical parameters typical for the large aspect ratio WEST tokamak [42] with inverse aspect ratio $a/R_0 = 0.2$, $B_0 = 3.7$ T, $R_0 = 2.5$ m. Equilibrium profiles are defined as:

$$q = 1 + (q_a - 1)x^2 \quad (46)$$

$$T_i = T_i^0 (1 - x^2)^2 \quad (47)$$

$$n_i = n_i^0 (1 - x^2) \quad (48)$$

with $x = r/a$, $T_i/T_e = 0.5$, $q_a = 4$, $T_e^0 = 3$ keV and $n_i^0 = 4 \times 10^{19} \text{ m}^{-3}$.

We show in figure 1 the profiles of the neoclassical coefficient k_i and of the normalized collisionality $\nu_{ji}^* = Rq / (\epsilon^{3/2} \tau_{ji} v_{Ti})$, with $v_{Ti} = (2T_i/m_i)^{1/2}$ and

$$\tau_{ji} = \frac{3\pi^{3/2} \epsilon_0^2 m_j^2 v_{Ti}^3}{e_i^2 e_j^2 n_i \ln \Lambda_{ji}} \quad (49)$$

The Coulomb logarithm $\ln \Lambda_{ji}$ is taken from the NRL formulary [43]. The banana regime corresponds to $\nu^* < 1$ and the Pfirsch-Schlüter regime to $\nu^* > \epsilon^{-3/2}$. The plateau regime is in between. We see that the main ions are marginally in the banana regime and this causes k_i to be larger than -1 . The ionization state of Tungsten that we will consider in the following, W^{44+} , is close to the boundary between the plateau and Pfirsch-Schlüter regimes in the plasma core ($r/a < 0.5$), and in the Pfirsch-Schlüter regime in the outer part of the plasma.

The pinch velocity and poloidal asymmetry derived from our model will be compared with the Fülöp-Helander model [26, 35] that describes the collisional transport and asymmetry of highly charged impurities ($Z_a \gg 1$), in a limit where the role of the impurity gradient in the flux is not taken into account, but where radial gradients of the ion species are considered in the parallel force balance, as in our model. The pinch velocity of the impurity given in eq. (36) of [35] can be expressed with our notations as:

$$V_{r,a}^{FH} = - \frac{Z_i}{Z_a} \frac{T_a}{e B_0 R_0 q^2} \mathcal{A} \mathcal{G}_0 \epsilon \left\{ 1 + (1 + M_0^2) \left(1 - \frac{\epsilon M_0^2}{C_\delta^0} \right) \frac{2q^2 (C_\delta^0)^2}{(\mathcal{A} \mathcal{G}_0 \epsilon)^2 + (C_\delta^0)^2} \right\} \quad (50)$$

with

$$M_0^2 = \frac{\delta_M}{2\epsilon} \left(1 - Z_a \frac{m_i}{m_a} \frac{T_e}{T_e + T_i} \right) \quad (51)$$

Here \mathcal{G}_0 corresponds to \mathcal{G} without the impurity pressure gradient. The latter is not present in this model because the diamagnetic rotation of the impurity, considered as

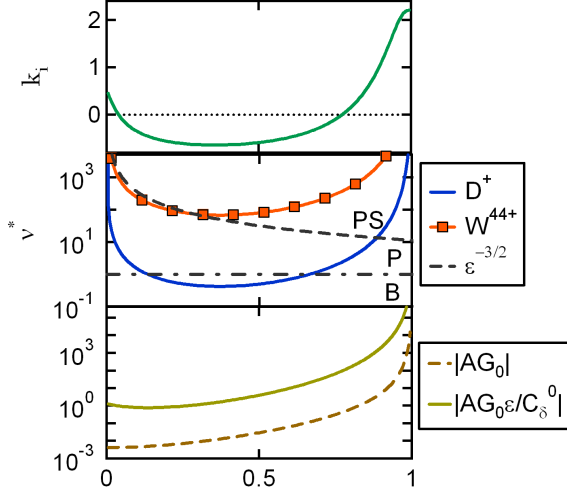


Figure 1. Neoclassical coefficient k_i (top) and collisionality regimes for the main ion species D^+ , W^{44+} (middle), and parameters $|\mathcal{AG}_0|$ and $|\mathcal{AG}_0\epsilon/C_\delta^0|$ (bottom) as a function of the plasma radius. The collisionality domains are labelled by 'B' for the banana regime, 'P' for the plateau regime and 'PS' for the Pfirsch-Schlüter regime.

small compared with the $\mathbf{E} \times \mathbf{B}$ rotation, is neglected. The asymmetry is expressed in this model as :

$$\delta^{FH} = 2C_\delta^0 \frac{(\mathcal{AG}_0\epsilon)^2 + \epsilon C_\delta^0 M_0^2}{(\mathcal{AG}_0\epsilon)^2 + (C_\delta^0)^2} \quad (52)$$

$$\Delta^{FH} = 2\mathcal{AG}_0\epsilon \frac{(C_\delta^0)^2 - \epsilon C_\delta^0 M_0^2}{(\mathcal{AG}_0\epsilon)^2 + (C_\delta^0)^2} \quad (53)$$

$$M_0^2 = \frac{\delta_M}{2\epsilon} \left(1 - Z_a \frac{m_i}{m_a} \frac{T_e}{T_e + T_i} \right) \quad (54)$$

This can be expressed in a geometrical representation as:

$$C_\delta^{FH} = C_\delta^0 + \epsilon M_0^2 \quad (55)$$

$$C_\Delta^{FH} = 0 \quad (56)$$

$$R_\Delta^{FH} = |C_\delta^0 - \epsilon M_0^2| \quad (57)$$

$$\cos \alpha^{FH} = \text{sign}(C_\delta^0 - \epsilon M_0^2) \frac{(\mathcal{AG}_0\epsilon)^2 - (C_\delta^0)^2}{(\mathcal{AG}_0\epsilon)^2 + (C_\delta^0)^2} \quad (58)$$

$$\sin \alpha^{FH} = \text{sign}(C_\delta^0 - \epsilon M_0^2) \frac{2(\mathcal{AG}_0\epsilon) C_\delta^0}{(\mathcal{AG}_0\epsilon)^2 + (C_\delta^0)^2} \quad (59)$$

In figure 1 (bottom plot), we display the radial profile of the parameter $|\mathcal{AG}_0|$ that represents the strength of collisional processes in the parallel force balance (RHS of equation (9) and parameter "g" in [35]), and the parameter $|\mathcal{AG}_0\epsilon/C_\delta^0|$ that represents the collisional titling amplitude (in the "natural" case discussed below, it

is approximately equal to the ratio δ/Δ). Although $|\mathcal{A}\mathcal{G}_0| \ll 1$ in the core region, meaning that the poloidal asymmetry of the impurity is small (for symmetric ϕ and without rotation), the tilting amplitude is larger than unity, meaning that the poloidal distribution (and therefore the impurity flux) can depart from conventional neoclassical theory predictions. Note that the difference between the two quantities $|\mathcal{A}\mathcal{G}_0|$ and $|\mathcal{A}\mathcal{G}_0\epsilon/C_\delta^0|$ comes from the ion temperature gradient contribution contained in parameter \mathcal{U} (see eq. (19)).

We will also compare our results with computations performed with the Drift-Kinetic code NEO [32]. NEO is based on the conventional neoclassical ordering [30] where radial gradients are assumed to be small (i.e. $|\mathcal{A}\mathcal{G}_0|$ small), and the RHS of the parallel force balance is neglected at lowest order. This contrast with the approach initiated by Helander and followed in the present model, where this assumption is relaxed. Additionally, the second order neoclassical flux computed in NEO, which is compared to our model, does not depend on the first order electrostatic potential and its associated asymmetries [32]. This results in an other fundamental difference since such asymmetries are accounted for in the computation of the impurity flux (eq. 33). NEO does not compute the classical flux, so that the comparison with our model requires considering the neoclassical flux only. The impurity profile from NEO at vanishing neoclassical flux can be deduced from $\partial_r \ln \langle n_a \rangle = V_a^{neo}/D_a^{neo}$, in the trace limit where the impurity concentration does not impact the main ion concentration. In our model, the neoclassical flux must be computed as a function of the impurity gradient to identify the stationary point and determine the neoclassical diffusion and pinch velocity, as well as the poloidal distribution of the impurity. NEO computations are performed using the full Fokker-Planck collision operator with 5 Laguerre and 17 Legendre polynomials. The circular geometry and kinetic electrons are also considered. The horizontal and vertical asymmetry parameters (δ , Δ) are obtained by fitting the poloidal distribution given by NEO with formula (11). The simplified description of poloidal asymmetries in the model limits its applicability to moderate deformation of the impurity distributions, namely $(\delta, \Delta) < 1$, and therefore the levels of toroidal Mach number and Hydrogen minority temperature anisotropy that can be studied.

3.1. The "natural" case

We consider first the situation where there is no toroidal rotation and no ICRF heating. In this case, if we assume that the electrostatic potential has no asymmetry, the neoclassical pinch can be strongly reduced by the self-consistent poloidal asymmetry when the impurity profile is flat [26]. This is illustrated in figure 2 (left plots) where the profiles of the classical ("cl."), neoclassical ("neo"), neoclassical without poloidal asymmetry ("neo.(0)") and total ("tot.") pinch velocities are shown, together with the asymmetry parameters (δ , Δ) of the impurity. This strong reduction of the flux occurs in the region where the collisional tilting is large (see figure 1), while the poloidal asymmetry remains small in amplitude.

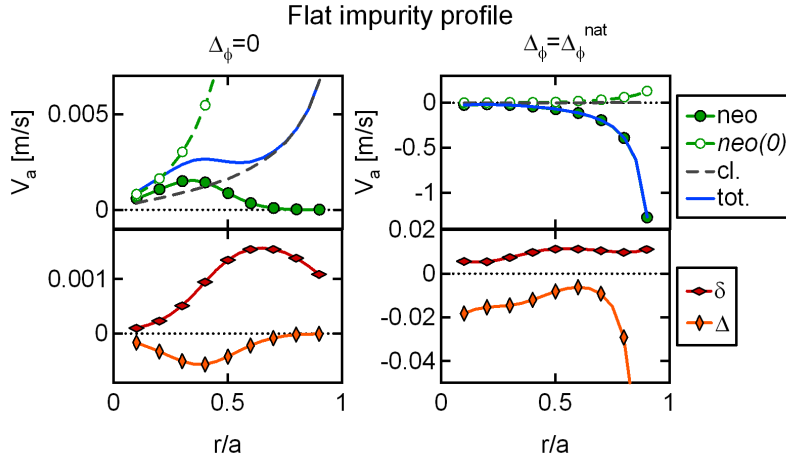


Figure 2. Natural case: profiles of the components of the pinch velocity, classical ("cl."), neoclassical ("neo"), neoclassical without poloidal asymmetry ("neo.(0)") and total ("tot.") (top plots), and poloidal asymmetry parameters (δ , Δ) (bottom plots) in a situation without (left plots) and with (right plots) the natural asymmetry of the electric potential determined from equation (41).

However, given the low amplitude of the poloidal asymmetry and the sensitivity of the flux on its amplitude, any residual asymmetry of the electrostatic potential can be instrumental in determining the impurity flux. The amplitude of the vertical asymmetry derived from equation (41), shown in the top plot of figure 5 for the plasma parameters considered here, is small in the plasma center but can reach several percents in the edge region. If we use this expression in the analytic model, we find a drastic change in the neoclassical pinch velocity: it becomes inward instead of outward, and much larger than the pinch evaluated at $\Delta_\phi = 0$ (figure 2, right plots).

The sensitivity of the impurity distribution on the poloidal asymmetry of the electrostatic potential is outlined in figure 3, where we show the contours of the total diffusion coefficient (classical plus neoclassical), pinch velocity, the horizontal and vertical asymmetries in the $(\delta_\phi, \Delta_\phi)$ plane at $r/a = 0.2$ for a flat impurity profile (left column) and at steady-state, i.e. when by changing the impurity gradient, the total collisional flux cancels (right column). The pinch velocity and diffusion coefficients show a nearly parabolic variation with respect to both δ_ϕ and Δ_ϕ . Note that, in this representation, minority ICRF heating ($T_\perp/T_\parallel > 1$) means a positive δ_ϕ .

The steady state is also strongly impacted by the asymmetry of the electrostatic potential. As shown in the right plots of figure 3, the pinch velocity and diffusion coefficient keep having a nearly parabolic variation in the $(\delta_\phi, \Delta_\phi)$ plane. In the absence of any source of horizontal asymmetry, the steady state value of δ remains close to zero at this radial position but the vertical asymmetry of the impurity reflects the amplitude of Δ_ϕ^{nat} , with an opposite sign. The consequence in terms of steady state normalized logarithmic impurity gradient (i.e. $\partial_x \ln n_a$ with $x = r/a$) is shown in figure 4 for W^{44+} at $r/a = 0.2$ and $r/a = 0.4$, where we find again a strong sensitivity with respect to the

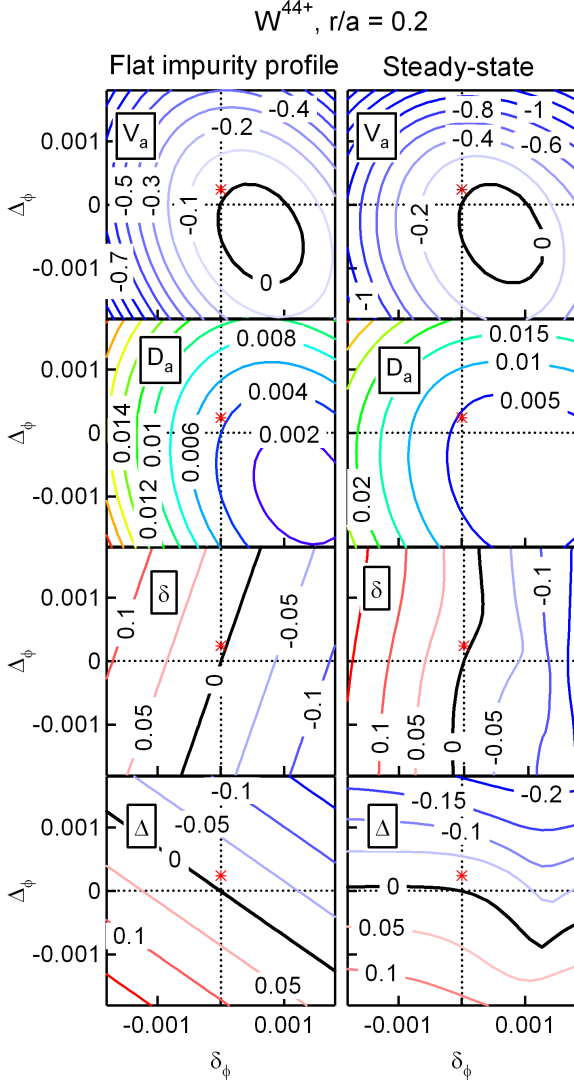


Figure 3. From top to bottom: contours of the total pinch velocity, diffusion coefficient, horizontal and vertical asymmetries for W^{44+} at $r/a = 0.2$ for a flat impurity profile (left) and at steady state (right), in the $(\delta_\phi, \Delta_\phi)$ plane. The natural asymmetry of the electrostatic potential given by equation (41) is shown with a red star.

natural vertical asymmetry Δ_ϕ^{nat} . It is interesting to note that the favourable region at $\Delta_\phi < 0$ cannot be accessed by reversing the sign of the magnetic field, which reverses the sign of Δ_ϕ^{nat} : by doing so, all the diagrams of figure 3 are reversed as well with respect to $\Delta_\phi = 0$, and the area with the most hollow steady state impurity profile in figure 4 remains out of reach.

The "natural" case is now addressed with the NEO code and compared with the analytical model at $\Gamma^{neo} = 0$. The profiles of the neoclassical pinch velocity and diffusion coefficient, asymmetry parameters and logarithmic impurity gradient found with the analytic model with and without Δ_ϕ^{nat} are shown in figure 5, together with the results from NEO. A variation of the vertical asymmetry Δ_ϕ^{nat} by 50% is also considered for

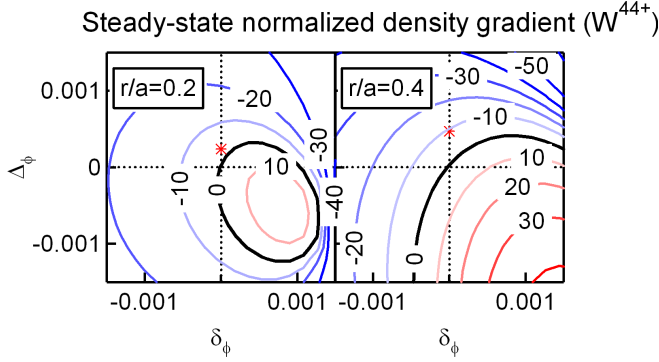


Figure 4. Normalized logarithmic density gradient ($\equiv \partial_x \ln n_a$) of W^{44+} at steady state ($\Gamma^{tot} = 0$), in the $(\delta_\phi, \Delta_\phi)$ plane at $r/a = 0.2$ and $r/a = 0.4$. The natural asymmetry of the electrostatic potential as given by equation (41) is shown with a red star.

evidencing its impact on the predictions of the model. In this "natural" case, the vertical asymmetry of the electrostatic potential at lowest order is zero in NEO, but it is finite at next order and agrees well with the formula of equation (41), as shown in figure 5 (top plot) [32]. However, the impurity flux is computed in NEO with the lowest order electrostatic potential (that is symmetric), and the importance of the vertical asymmetry in the "natural" case leads to inevitable differences in the evaluation of the impurity transport. In the limit $\Delta_\phi = 0$ used in NEO for the computation of the flux, diffusion coefficients from the model and NEO are in excellent agreement, but the pinch velocity is clearly inward in NEO, while it is outward and much smaller in the model. In this respect, the relative agreement between the prediction of the model with Δ_ϕ^{nat} and NEO in the central region of the plasma might just be a coincidence. The poloidal impurity asymmetry given in the NEO output takes into account Δ_ϕ^{nat} but ignores the collisional tilting due to the friction force from equation (9). It is therefore purely vertical, while the model predicts a remaining coupling between the two asymmetry components at steady state. This coupling is visible in figure 3 ($r/a = 0.2$), and it is more pronounced at larger radius where Δ_ϕ^{nat} and the friction force become larger. Globally speaking, we conclude that the predictions from the analytical model and from NEO disagree in the "natural" case. This comes from two components entering the neoclassical flux computations that are not included in the standard neoclassical ordering used in NEO, namely the induced asymmetry from the first order electrostatic potential and the tilting term.

3.2. Effect of toroidal rotation

3.2.1. Pinch velocity and poloidal asymmetry We first consider the case of a flat impurity profile. This allows, in the case of toroidal rotation, a comparison with the Fülöp-Helander model that does not address the steady state solution. A scan in the ion Mach number is performed for W^{44+} at $r/a = 0.2$, a region of the plasma where

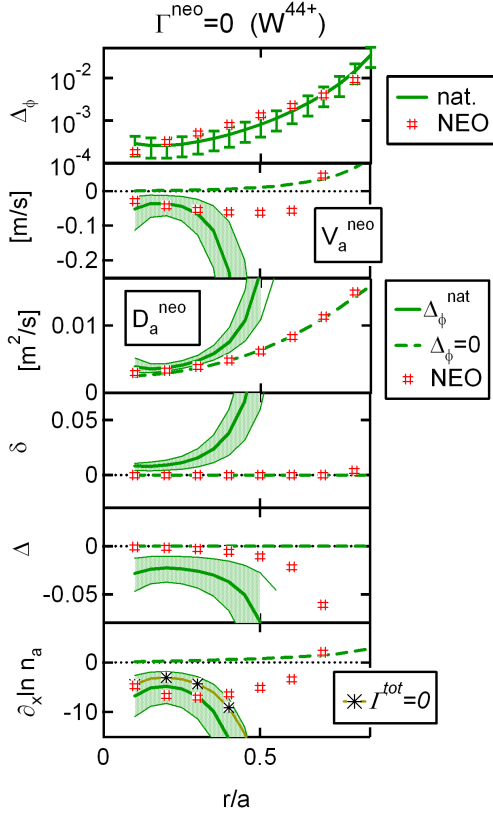


Figure 5. From top to bottom: vertical asymmetry of the electrostatic potential, neoclassical pinch velocity and diffusion coefficient, horizontal and vertical asymmetry and normalized logarithmic density gradient ($\partial_x \ln n_a$) at $\Gamma^{neo} = 0$ for W^{44+} with and without the natural vertical asymmetry of the electrostatic potential, as a function of the minor radius. The shaded area indicates the variation of these parameters when Δ_ϕ^{nat} is varied by 50%. Results from NEO are shown with hastags and the solution at $\Gamma^{tot} = 0$ is indicated in the bottom plot.

neoclassical transport can easily overcome turbulent transport. We show in figure 6 the pinch velocity, diffusion coefficient, and the asymmetry parameters (δ, Δ) as a function of M_i . Toroidal rotation is shown to drive a strong inward pinch, as well as a large diffusion coefficient. The horizontal asymmetry becomes positive as a result of the centrifugal force, but the vertical asymmetry is also significant, although with a lower amplitude. The pinch velocity and the poloidal asymmetry predicted by the Fülöp-Helander model are in excellent agreement with our model. We also display for comparison the result of NEO calculations in the same figure 6. We will discuss later (section 3.2.2) the evolution of these parameters with the impurity gradient, but we can notice here the relatively good match of the pinch and diffusion coefficient for $M_i < 0.3$ despite the imperfect match of the poloidal asymmetry, in particular its vertical component.

We can also illustrate the evolution of the poloidal asymmetry using a geometrical representation, as shown in figure 7. A larger Mach number translates into an ellipsis with larger dimensions. We note that the circle moves away from the symmetric point

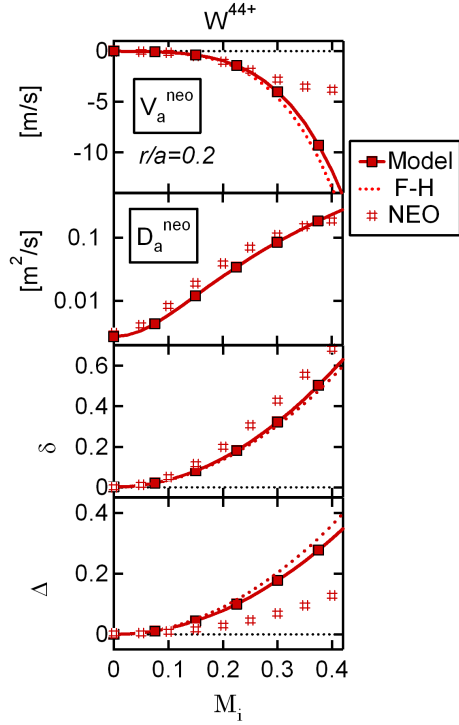


Figure 6. From top to bottom: neoclassical pinch velocity, diffusion coefficient, horizontal and vertical asymmetries for a flat radial profile of W^{44+} at $r/a = 0.2$, as a function of the ion Mach number. Dotted lines correspond to the Fülöp-Helander model (F-H) and hashtags to NEO (steady state) results.

$(\delta, \Delta) = (0, 0)$ in the direction of larger δ as the ion Mach number increases, a feature that is not captured by the Fülöp-Helander model. This gap is precisely $2\mathcal{F}$ and increases with toroidal rotation (see equation 20), while it is simply $2C_\delta^0 \approx 6 \times 10^{-4}$ in the Fülöp-Helander model. This can lead to a discrepancy in the horizontal asymmetry prediction between the two models for a large value of $|\mathcal{AG}_0|$ (highly charged impurities, low ion temperature or large gradients). As an example we show in figure 8 the asymmetry reconstruction for $T_i/T_e = 0.2$ instead of 0.5. The collisional angle α being close to 180° , the vertical asymmetry is comparable for the two models, while the difference in the predicted horizontal asymmetry is large.

Figure 7 also shows that, as the ion Mach number is increased, the asymmetry parameters follow a trajectory that is quasi linear (black line for our model, and dotted line for the Fülöp-Helander model). It is in fact exactly linear in the Fülöp-Helander model since we have

$$\Delta^{FH} = (\delta^{FH} - C_\delta^{FH}) \frac{2(\mathcal{AG}_0\epsilon) C_\delta^0}{(\mathcal{AG}_0\epsilon)^2 - (C_\delta^0)^2} \quad (60)$$

where the toroidal rotation effect is contained in C_δ^{FH} . For the model derived here, we

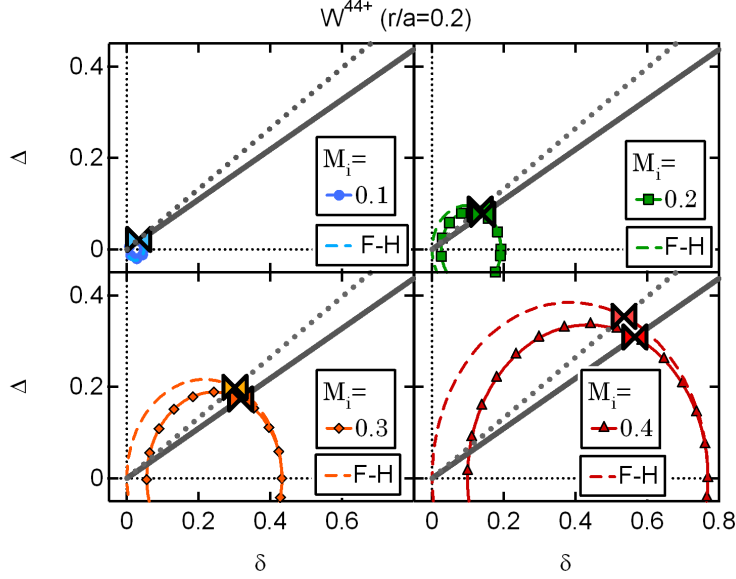


Figure 7. Geometrical representation of the elliptic curves (δ, Δ) for different values of the ion Mach number, trajectory followed during the scan in M_i (full line), and actual positions at their intersection (\times), for W^{44+} at $r/a = 0.2$. The prediction from the Fülöp-Helander model are also shown (colored dashed lines, grey dots and \times symbol respectively).

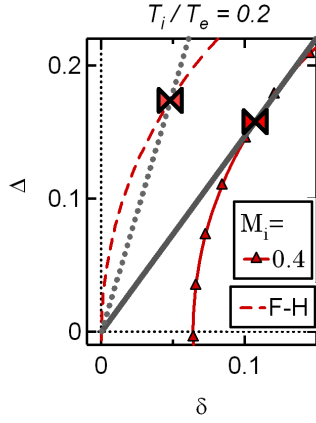


Figure 8. Geometrical representation of the elliptic curves (δ, Δ) for $M_i = 0.4$ and $T_i/T_e = 0.2$ (same legend as figure 7).

also have a linear relation for $\Delta_N = \Delta_\phi = 0$, provided $\mathcal{H} \approx 1$ since we then have:

$$\Delta = (\delta - C_\delta) \frac{2(\mathcal{AG}\epsilon) C_\delta^0}{(\mathcal{AG}\epsilon)^2 \mathcal{H} - (C_\delta^0)^2} \quad (61)$$

3.2.2. Steady-state impurity profile The logarithmic density gradient at $\Gamma^{neo} = 0$ is shown as a function of the ion Mach number in figure 9 for W^{44+} at $r/a = 0.2$. The core accumulation of the charged impurity ions is rapidly growing and tends to saturate

above $M_i \sim 0.2$. The poloidal asymmetry is characterized by a large accumulation on the low field side of the plasma, with an horizontal asymmetry that increases with M_i , while the vertical asymmetry is nearly zero. When the natural vertical asymmetry of the electrostatic potential is added, the impurity gradient at low rotation is moving towards more negative values, but the solution at $M_i > 0.1$ is not affected, apart from the vertical asymmetry that has a small remaining negative value. The agreement with NEO is good for Tungsten diffusion and pinch velocity, as well as for the horizontal asymmetry, up to $M_i \sim 0.3$. At low Mach number, taking into account the natural vertical asymmetry of the electrostatic potential improves the matching, with a Tungsten density gradient that remains negative as $M_i \rightarrow 0$, although the reason for this better agreement is not well understood, as explained earlier. For toroidal rotation larger than $M_i \sim 0.3$, the horizontal asymmetry approaches 100% and cannot be fitted accurately with (δ, Δ) . The comparison with figure 6 outlines the dependence of the poloidal asymmetry on the impurity profile since the horizontal asymmetry from the model and from NEO are now in perfect agreement. The vertical asymmetry vanishes almost exactly following the model predictions with $\Delta_\phi = 0$, while the fit of $n_a(\theta)/\langle n_a \rangle$ from NEO still identifies a small remaining positive contribution.

The details of the variation of the radial velocity and poloidal asymmetry with the impurity gradient is shown in figure 10 for $\Delta_\phi = 0$. Toroidal rotation strongly enhances the inward neoclassical impurity pinch so that the weight of the classical flux is negligible above $M_i = 0.1$. This figure also illustrates the variation of the poloidal asymmetry with the impurity gradient, with an horizontal asymmetry that increases as $\partial_x \ln n_a$ is evolving from zero to steady state, while the vertical asymmetry practically vanishes when assuming $\Delta_\phi = 0$.

3.3. Effect of anisotropic minority ion temperature

We now consider the case of ICRH-driven temperature anisotropy, with 10% of Hydrogen minority, and a minority temperature anisotropy T_\perp/T_\parallel ranging from 1 to 4. The scan is extended to $T_\perp/T_\parallel \in [0, 1]$, a range that is not relevant for ICRH but connects with the figures of section 3.1. This temperature anisotropy is used in equation (40) to compute the horizontal asymmetry of the electrostatic potential. The parameter $f_H(T_\perp/T_\parallel - 1)$, representative of δ_ϕ variation, varies up to 0.3, a value that is typical in experimental situations [16]. The dependence of the neoclassical velocity pinch, diffusion coefficient and asymmetry parameters on T_\perp/T_\parallel is shown in figure 11 for a flat impurity profile. The horizontal asymmetry is driven negative by a dominant perpendicular minority temperature, as observed experimentally [44, 16, 18, 31, 20]. At the same time, the pinch velocity follows a nearly parabolic curve: it moves to the outward direction first, and then becomes more inward again. This reversal of the flux is obtained with a moderate level of electrostatic potential anisotropy for Tungsten due to its large electric charge (see also figure 3 of [29]). The computation has been done for $\Delta_\phi = 0$ but also for $\Delta_\phi = \Delta_\phi^{nat}$, where we assume for simplicity that this imposed vertical asymmetry

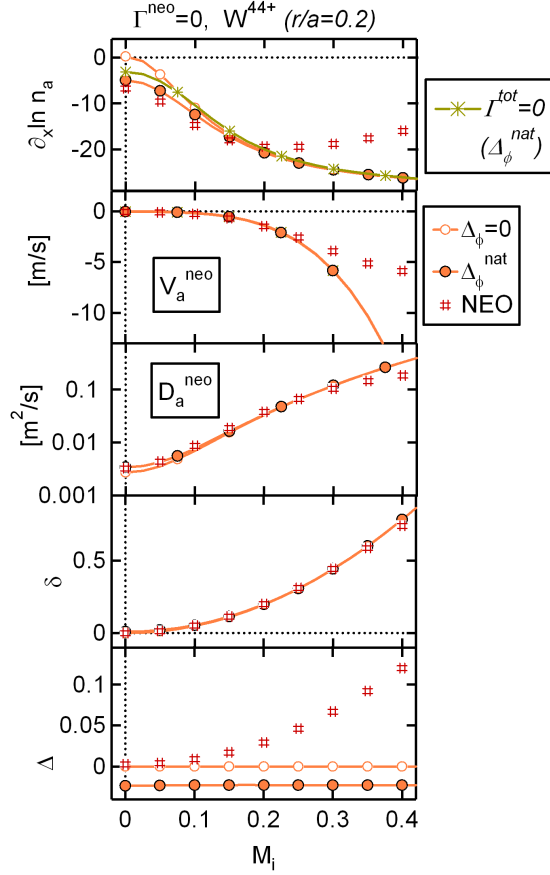


Figure 9. From top to bottom: normalized logarithmic impurity density gradient, neoclassical pinch velocity, diffusion coefficient, horizontal and vertical asymmetries at $\Gamma^{neo} = 0$ as a function of the ion Mach number, at $r/a = 0.2$ for W^{44+} , with $\Delta_\phi = 0$ and $\Delta_\phi = \Delta_\phi^{nat}$. The results from NEO are shown with hashtags symbols. We also show the steady state solution including classical transport and $\Delta_\phi = \Delta_\phi^{nat}$ on the top plot ($\Gamma^{tot} = 0$).

of the electrostatic potential does not impact the poloidal distribution of the minority ions. The impact is limited to a shift in the vertical asymmetry of the impurity and a change of the pinch and diffusion at low T_\perp/T_\parallel that will appear more clearly when computing impurity gradient at vanishing flux. We show on the same plot the results obtained with the NEO code (hashtags symbols in figure 11). The pinch velocity and diffusion coefficient computed with NEO are in good agreement with the ones obtained with the model. It is worth noting that, at the temperature anisotropy that minimizes the diffusion coefficient (around $T_\perp/T_\parallel \approx 2$), the neoclassical diffusion is below the classical one. The horizontal asymmetry is also in good agreement between the two approaches, but a large mismatch can be noted on the vertical asymmetry, due to the absence of the collisional tilting effect in NEO. Taking into account the natural vertical asymmetry Δ_ϕ^{nat} has little effect except in the domain of low diffusion where it adds a small contribution, and as for the rotation case, it slightly shifts the vertical asymmetry

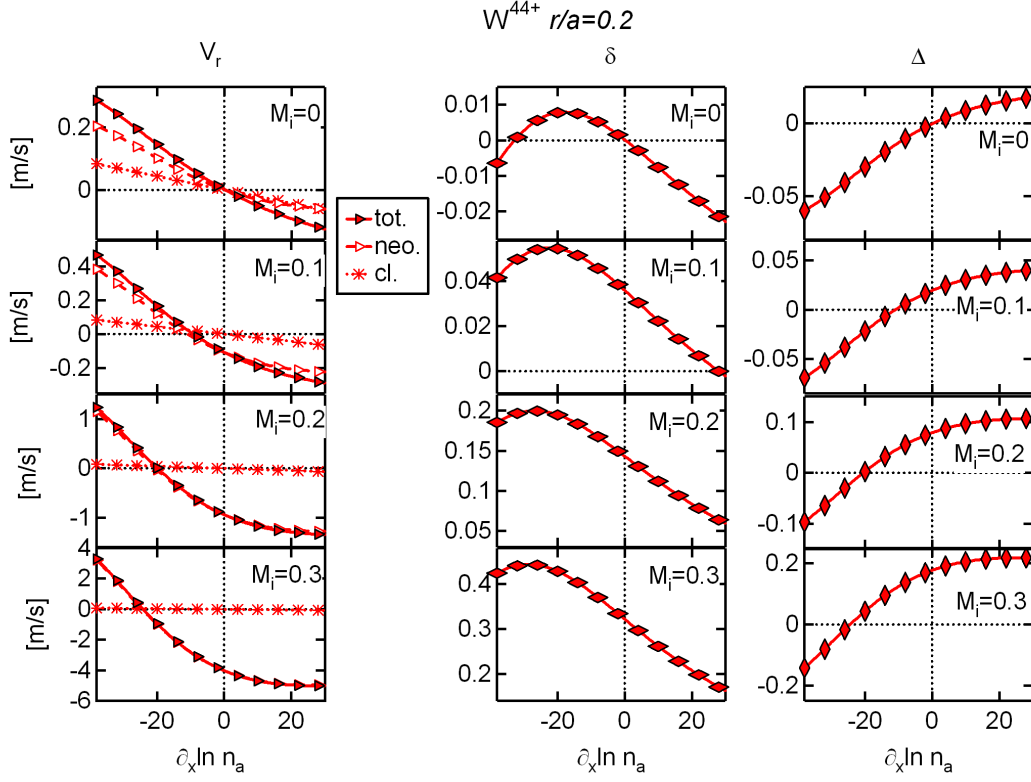


Figure 10. Total, neoclassical and classical impurity flow (left), horizontal (middle) and vertical (right) asymmetry, as a function of the logarithmic impurity gradient for different values of the ion Mach number, for W^{44+} at $r/a = 0.2$ ($\Delta_\phi = 0$).

of the impurity downwards.

3.3.1. Steady-state impurity distribution in the case of anisotropic minority ion temperature We show in figure 12 the neoclassical steady state value ($\Gamma^{neo} = 0$) of the logarithmic density gradient of W^{44+} at $r/a = 0.2$, as a function of T_\perp/T_\parallel . We find that except in a limited range of T_\perp/T_\parallel values just above unity, the asymmetry of the electrostatic potential induced by ICRH leads to impurity accumulation in the core. The region around $T_\perp/T_\parallel \sim 2$ is particular. Indeed, the neoclassical diffusion coefficient is vanishing around $T_\perp/T_\parallel \sim 2$ when the natural asymmetry of ϕ is neglected so that the neoclassical flux cannot be cancelled by changing the impurity gradient. This gives a divergence in the steady state Tungsten density gradient (top plot). The contribution of the classical flux is then essential. This divergence is also removed when we take $\Delta_\phi = \Delta_\phi^{nat}$ because the minimum of the neoclassical diffusion is not as low as with $\Delta_\phi = 0$. The horizontal asymmetry at steady state is decreasing quasi-linearly with T_\perp/T_\parallel , being positive for $T_\perp/T_\parallel < 1$ and negative for $T_\perp/T_\parallel > 1$. The vertical asymmetry is slightly negative with a minimum of a few percents for T_\perp/T_\parallel between 2 and 4, and goes back towards zero as T_\perp/T_\parallel increases further. Computations with NEO show a good agreement, with a comparable steady state impurity gradient. In particular,

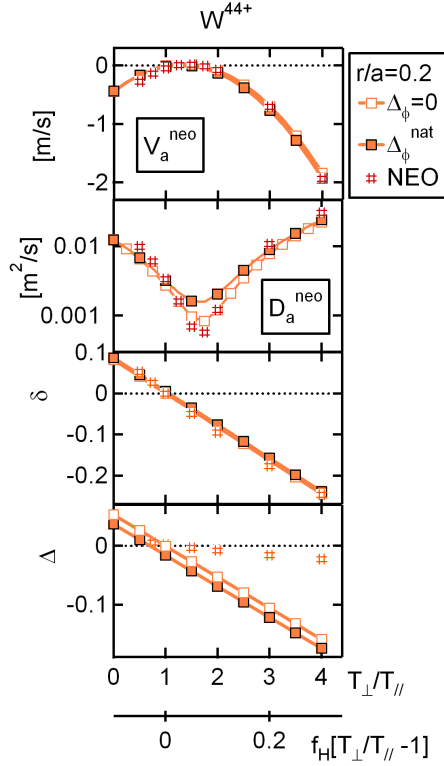


Figure 11. From top to bottom: neoclassical pinch velocity and diffusion coefficient, horizontal and vertical asymmetries for a flat profile of W^{44+} at $r/a = 0.2$, as a function of the Hydrogen temperature anisotropy T_{\perp}/T_{\parallel} and of $f_H(T_{\perp}/T_{\parallel} - 1)$. Results from the code NEO are shown for comparison.

the transition between a positive density gradient (hollow impurity profile) for T_{\perp}/T_{\parallel} just above unity to a large negative gradient (peaked impurity profile) is also found. The horizontal asymmetry is in good agreement between the model and NEO and, in contrast with the transient case with a flat impurity profile (see figure 11), the vertical asymmetry is small and negative in the two cases. The steady state characteristics are weakly dependent on the natural vertical asymmetry of the electrostatic potential, also shown in the figure.

The variation of the collisional flux and poloidal asymmetry of W^{44+} with the impurity gradient is detailed in figure 13 for increasing temperature anisotropy. For $T_{\perp}/T_{\parallel} \sim 2$, the neoclassical flux is small and nearly independent from the impurity gradient, which gives particular importance to the classical flux, as mentioned earlier. The figure also shows that the variation of the asymmetry with the impurity gradient can be relatively large, as evidenced also by the comparison between figures 11 and 12.

The result that ICRH can lead to Tungsten accumulation seems to contradict experimental analyses where on the contrary ICRH was found to be beneficial for impurity removal from the core plasma [45, 14, 19, 20, 21]. In these experimental

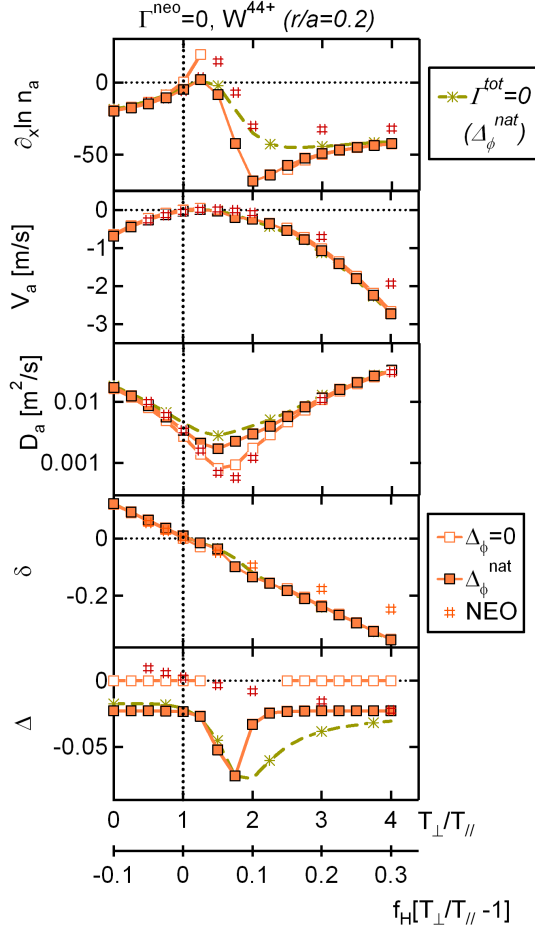


Figure 12. From top to bottom, as a function of the minority ion temperature anisotropy: normalized logarithmic impurity gradient, neoclassical pinch velocity and diffusion coefficient, horizontal and vertical asymmetries at $\Gamma^{neo} = 0$ for W^{44+} at $r/a = 0.2$, with $\Delta_\phi = 0$ and $\Delta_\phi = \Delta_\phi^{nat}$. The steady state impurity gradient obtained by cancelling the total flux ($\Gamma^{tot} = 0$) at $\Delta_\phi = \Delta_\phi^{nat}$ is also indicated, and the results from NEO are shown with hashtags symbols.

cases however, several additional effects should be considered. First, ICRH provides ion and electron heating that are not considered in our analysis. These heatings have an impact on the neoclassical transport: thermal screening via ion temperature increase, as well as lower peaking via the change of the electron density profile induced by the modified turbulent transport properties [20, 21]. Second, the friction of the impurity with the minority species provides an additional screening effect that is not considered here (temperature and density gradients of fast ions were set to zero) [14, 20]. Moreover, these experimental results were also obtained in a situation where ICRH was combined with toroidal rotation. And the variation of horizontal asymmetry induced by ICRH opposes that due to toroidal rotation, thus reducing the steady state Tungsten accumulation. This issue is illustrated in figure 14 where we scan both the ion Mach

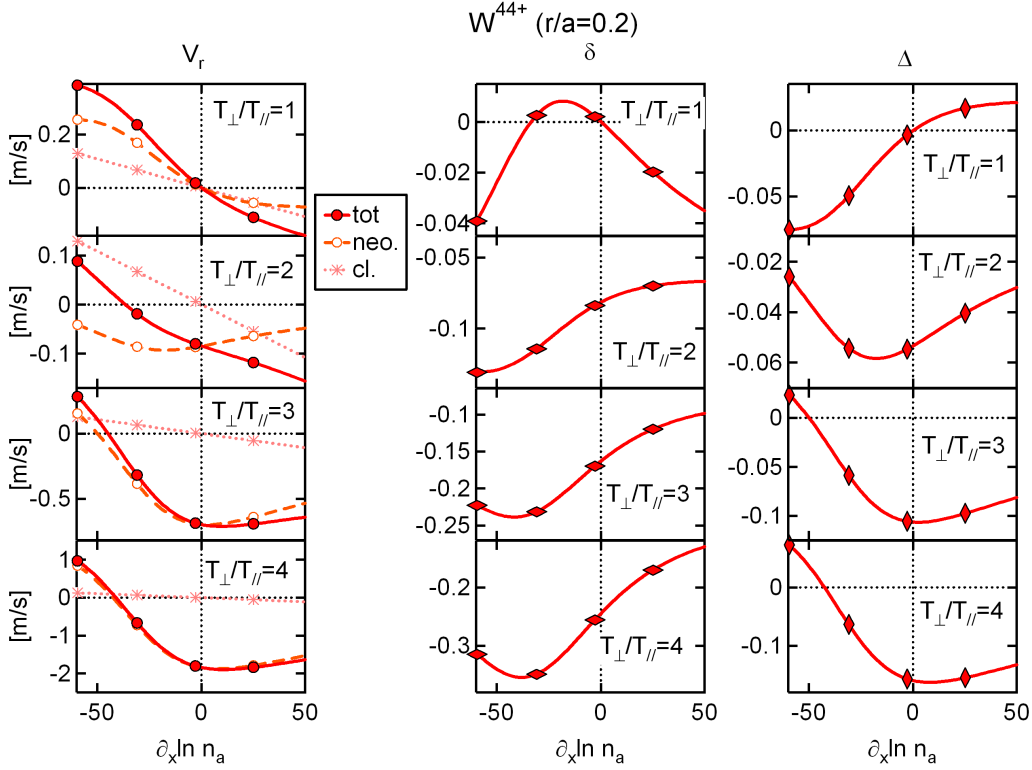


Figure 13. Total, neoclassical and classical impurity flux (left), horizontal (middle) and vertical (right) asymmetries as a function of the logarithmic impurity gradient for different values of the minority ion temperature anisotropy, for W^{44+} at $r/a = 0.2$ ($\Delta_\phi = 0$).

number and the ratio T_\perp/T_\parallel to determine the steady state gradient together with the poloidal asymmetry parameters of W^{44+} at $r/a = 0.2$. The favourable window in T_\perp/T_\parallel where Tungsten is expelled moves to higher values as toroidal rotation is increased. At finite ion Mach number, increasing the minority ion temperature anisotropy leads in the first place to a reduction of impurity accumulation, consistent with experimental observations. Increasing T_\perp/T_\parallel above the range where the impurity is expelled should lead however to an abrupt transition to a regime of strong accumulation that has not been encountered (or documented) so far in experiments. This critical value can be estimated by considering the following points:

- (i) the transition in the steady state impurity peaking seems closely related with the minimum of the neoclassical diffusion coefficient (see figure 12), i.e. for $\delta/\epsilon \approx -2$ (see eq. 36)
- (ii) the collisional tilting of the poloidal asymmetry (RHS of equation 16) is about its minimum value at steady state (the vertical asymmetry is about zero when the drive is horizontal), so that we have $\delta \approx -\delta_\phi^a + \delta_M$

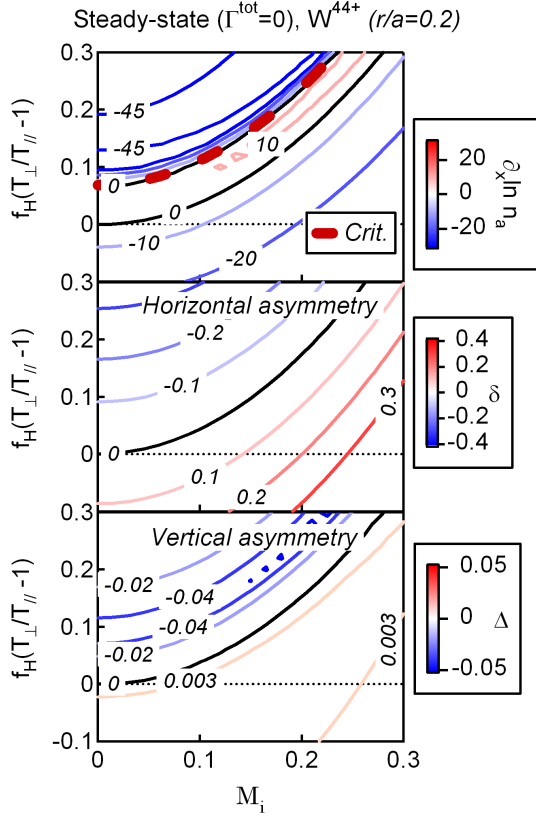


Figure 14. From top to bottom: steady state normalized logarithmic W^{44+} gradient, horizontal and vertical asymmetry, as a function of the ion Mach number and of the parameter $f_H(T_{\perp}/T_{\parallel} - 1)$ at $r/a = 0.2$ and with $\Delta_{\phi} = 0$. The critical anisotropy given by equation (62) is shown with the red dashed line.

This gives the following estimate:

$$\left[f_H \left(\frac{T_{\perp}}{T_{\parallel}} - 1 \right) \right]^{crit} \approx 2 \frac{Z_i + T_i/T_e}{Z_a} + 2M_i^2 \left[\frac{m_a}{m_i} \frac{Z_i + T_i/T_e}{Z_a} - 1 \right] \quad (62)$$

This estimate is shown in figure 14 with a red dashed line, and falls close to the level of anisotropy that leads to impurity accumulation.

4. Conclusion

We have derived in this paper a simplified analytic formulation of the self-consistent problem of poloidal impurity distribution and radial flux in the Pfirsch-Schlüter regime, covering the effect of anisotropic electrostatic potential and of toroidal rotation. This work extends earlier findings that the poloidal distribution can be formulated in a geometric representation [29]. The poloidal asymmetry varies in particular with the impurity gradient via the combination of the diamagnetic velocity and the friction force, adding a nonlinear dependence of the flux on the impurity gradient through the poloidal distribution that is not assumed in standard neoclassical theory. Three applications of

experimental interest ("natural" case, toroidal rotation and ICRH heating) have been considered, and the predictions of the model have been compared with earlier works applicable to a flat impurity profile [26, 35], where a good agreement is found, and with computations of the steady state using the NEO code [32].

Focusing on the comparison with NEO, evaluated at the cancellation of the neoclassical flux, we reported a satisfactory agreement with the neoclassical diffusion, pinch velocity and poloidal asymmetry of Tungsten for a toroidal plasma rotation raising up to a ion Mach number of about 0.3. Regarding ICRH heating, a good agreement is also found, with a Tungsten profile that tends to be flat or hollow at moderate temperature anisotropy, reflecting the beneficial effect of ICRH heating reported in experimental observations. But both our model and NEO are predicting a strong accumulation above some critical value, for which an analytical estimate is given. To our knowledge, this situation has not been reported so far in experimental analyses. The reason may be that this accumulation is compensated, fully or partly, by additional thermal screening from the minority species [14], not considered here, or that toroidal rotation is always sufficiently strong to push this situation outside the accessible range in experiments. Another interesting result found when applying the model to ICRH heating is that retaining the classical flux in addition to the neoclassical one can be important for determining the steady-state impurity gradient in particular ranges of parameters where the neoclassical diffusion coefficient can be nearly suppressed by the self-consistent poloidal asymmetry of the impurity. The results obtained with our analytical model indicate that the steady state impurity profile tends to minimize the contribution of the collisional terms in the parallel force balance, so that the horizontal asymmetry drive from toroidal rotation or ICRH heating results in a nearly pure horizontal asymmetry of the impurity distribution, which is not the case as long as the collisional flux is finite. To this respect, the conventional neoclassical ordering used in NEO seems to be justified in the steady state regime.

In the "natural" case (no toroidal rotation and no ICRH heating), we have shown that even a small residual asymmetry of the electrostatic potential can considerably change the steady state impurity gradient. This sensitivity has been evidenced here with respect to the positive vertical asymmetry of the electrostatic potential driven by collisions. It is proportional to the ion temperature gradient and drives an inward pinch. We note that a significant contribution of the electrostatic potential asymmetry to the poloidal distribution of highly charged impurities was also outlined in PIC simulations with the XGCa code [37]. The amplitude of this effect decreases at low collisionality, and becomes subdominant as soon as a sufficiently large external source of poloidal asymmetry is considered, for example, when the ion Mach number exceeds few percents. This "natural" case appears as the most critical in the comparison with NEO. The vertical asymmetry of the electrostatic potential that plays such an important role is indeed computed as a secondary order term (where it is consistent with theory) and is not used for the computation of the impurity flux. The friction force between the impurity and the main ions plays a large role in the poloidal distribution, and transfers the vertical

asymmetry of the electrostatic potential in a combination of vertical and horizontal asymmetries of the impurity, a transfer that is not described in the conventional ordering of neoclassical theory. Note that a turbulence driven asymmetry of the electrostatic potential adds to the collision drive. It also generates an asymmetry of the impurity distribution that is not purely vertical, an horizontal component being driven by the ballooning of the turbulent Reynolds stress [46, 47, 48].

The model described in this paper, being able to describe transient situations where the impurity is still evolving towards steady state, can be of interest for integrated simulation purposes, where the time scale of collisional transport competes with turbulent one, as well as with the dynamics of radiation losses and equilibrium evolution. Its formulation allows a fast computation (by 6 orders of magnitude compared with NEO) although the geometrical simplifications (circular plasmas) and collisional range of application limits its accuracy in its present form.

Acknowledgments

This work has been carried out within the framework of the French Research Federation for Fusion Studies, and of the EUROfusion Consortium. It has received funding from the Euratom research and training programme 2014-2018 and 2019-2020 under grant agreement No 633053 for the project ENR-MFE19.CEA-03. The views and opinions expressed herein do not necessarily reflect those of the European Commission. The authors thank in particular one of the referees for very constructive comments that greatly improved the text.

References

- [1] R Guirlet, C Giroud, T Parisot, M E Puiatti, C Bourdelle, L Carraro, N Dubuit, X Garbet, and P R Thomas. Parametric dependences of impurity transport in tokamaks. Plasma Physics and Controlled Fusion, 48(12B):B63–B74, nov 2006.
- [2] T Parisot, R Guirlet, C Bourdelle, X Garbet, N Dubuit, F Imbeaux, and P R Thomas. Experimental impurity transport and theoretical interpretation in a Tore Supra lower-hybrid heated plasma. Plasma Physics and Controlled Fusion, 50(5):055010, apr 2008.
- [3] D. Villegas, R. Guirlet, C. Bourdelle, G. T. Hoang, X. Garbet, and R. Sabot. Experimental electron temperature gradient dependence of heavy impurity transport in fusion devices. Phys. Rev. Lett., 105:035002, Jul 2010.
- [4] R. D. Petrasso, D. J. Sigmar, K. W. Wenzel, J. E. Hopf, M. Greenwald, J. L. Terry, and J. Parker. Observations of Centrally Peaked Impurity Profiles Following Pellet Injection in the Alcator-C Tokamak. Phys. Rev. Lett., 57:707–710, Aug 1986.
- [5] P.C Efthimion, S. Von Goeler, W.A Houlberg, E.J Synakowski, M.C Zarnstorff, S.H Batha, R.E Bell, M Bitter, C.E Bush, F.M Levinton, E Mazzucato, D.C McCune, D Mueller, H.K Park, A.T Ramsey, A.L Roquemore, and G Taylor. Observation of neoclassical transport in reverse shear plasmas on TFTR. Nuclear Fusion, 39(11Y):1905–1909, nov 1999.
- [6] T. Sunn Pedersen, R.S Granetz, A.E Hubbard, I.H Hutchinson, E.S Marmor, J.E Rice, and J Terry. Radial impurity transport in the H mode transport barrier region in Alcator C-Mod. Nuclear Fusion, 40(10):1795–1804, oct 2000.

- [7] J.E. Rice, P.T. Bonoli, E.S. Marmar, S.J. Wukitch, R.L. Boivin, C.L. Fiore, R.S. Granetz, M.J. Greenwald, A.E. Hubbard, J.W. Hughes, I.H. Hutchinson, J.H. Irby, Y. Lin, D. Mossessian, M. Porkolab, G. Schilling, J.A. Snipes, and S.M. Wolfe. Double transport barrier plasmas in Alcator C-Mod. Nuclear Fusion, 42(5):510–519, may 2002.
- [8] T. Pütterich, R. Dux, M.A. Janzer, and R.M. McDermott. ELM flushing and impurity transport in the H-mode edge barrier in ASDEX Upgrade. Journal of Nuclear Materials, 415(1, Supplement):S334 – S339, 2011. Proceedings of the 19th International Conference on Plasma-Surface Interactions in Controlled Fusion.
- [9] K. Ida, R. J. Fonck, S. Sesnic, R. A. Hulse, and B. LeBlanc. Observation of z-dependent impurity accumulation in the PBX tokamak. Phys. Rev. Lett., 58:116–119, Jan 1987.
- [10] J.A Wesson. Poloidal distribution of impurities in a rotating tokamak plasma. Nuclear Fusion, 37(5):577–581, may 1997.
- [11] J. E. Rice, J. L. Terry, J. A. Goetz, Y. Wang, E. S. Marmar, M. Greenwald, I. Hutchinson, Y. Takase, S. Wolfe, H. Ohkawa, and A. Hubbard. Impurity transport in Alcator C-Mod plasmas. Physics of Plasmas, 4(5):1605–1609, 1997.
- [12] M Romanelli and M Ottaviani. Effects of density asymmetries on heavy impurity transport in a rotating tokamak plasma. Plasma Physics and Controlled Fusion, 40(10):1767–1773, oct 1998.
- [13] C. Angioni, P. Mantica, T. Pütterich, M. Valisa, M. Baruzzo, E.A. Belli, P. Belo, F.J. Casson, C. Challis, P. Drewelow, C. Giroud, N. Hawkes, T.C. Hender, J. Hobirk, T. Koskela, L. Lauro Taroni, C.F. Maggi, J. Mlynar, T. Odstrcil, M.L. Reinke, M. Romanelli, and JET EFDA Contributors. Tungsten transport in JET H-mode plasmas in hybrid scenario, experimental observations and modelling. Nuclear Fusion, 54(8):083028, 2014.
- [14] F J Casson, C Angioni, E A Belli, R Bilato, P Mantica, T Odstrcil, T Pütterich, M Valisa, L Garzotti, C Giroud, J Hobirk, C F Maggi, J Mlynar, and M L Reinke. Theoretical description of heavy impurity transport and its application to the modelling of tungsten in JET and ASDEX upgrade. Plasma Physics and Controlled Fusion, 57(1):014031, nov 2015.
- [15] V.S. Chan, S.C. Chiu, and S.K. Wong. Impurity transport in ICRH tokamak plasma. Nuclear Fusion, 25(6):697–704, jun 1985.
- [16] M L Reinke, I H Hutchinson, J E Rice, N T Howard, A Bader, S Wukitch, Y Lin, D C Pace, A Hubbard, J W Hughes, and Y Podpaly. Poloidal variation of high-Zimpurity density due to hydrogen minority ion cyclotron resonance heating on Alcator C-Mod. Plasma Physics and Controlled Fusion, 54(4):045004, mar 2012.
- [17] Ye O Kazakov, I Pusztai, T Fülöp, and T Johnson. Poloidal asymmetries due to ion cyclotron resonance heating. Plasma Physics and Controlled Fusion, 54(10):105010, aug 2012.
- [18] R. Bilato, O. Maj, and C. Angioni. Modelling the influence of temperature anisotropies on poloidal asymmetries of density in the core of rotating plasmas. Nuclear Fusion, 54(7):072003, apr 2014.
- [19] A. Loarte, M. L. Reinke, A. R. Polevoi, M. Hosokawa, M. Chilenski, N. Howard, A. Hubbard, J. W. Hughes, J. E. Rice, J. Walk, F. Kehl, T. Pütterich, R. Dux, and V. E. Zhogolev. Tungsten impurity transport experiments in Alcator C-Mod to address high priority research and development for ITER. Physics of Plasmas, 22(5):056117, 2015.
- [20] M Goniche, R J Dumont, V Bobkov, P Buratti, S Brezinsek, C Challis, L Colas, A Czarnecka, P Drewelow, N Fedorczak, J Garcia, C Giroud, M Graham, J P Graves, J Hobirk, P Jacquet, E Lerche, P Mantica, I Monakhov, P Monier-Garbet, M F F Nave, C Noble, I Nunes, T Pütterich, F Rimini, M Sertoli, M Valisa, and D Van Eester and. Ion cyclotron resonance heating for tungsten control in various JET H-mode scenarios. Plasma Physics and Controlled Fusion, 59(5):055001, mar 2017.
- [21] C. Angioni, M. Sertoli, R. Bilato, V. Bobkov, A. Loarte, R. Ochoukov, T. Odstrcil, T. Pütterich, and J. Stober and. A comparison of the impact of central ECRH and central ICRH on the tungsten behaviour in ASDEX Upgrade H-mode plasmas. Nuclear Fusion, 57(5):056015, mar 2017.
- [22] M Z Tokar, T Baelmans, V Philipps, D Reiter, U Samm, B Unterberg, H A Classen, H Gerhauser,

- J D Hey, A Huber, P Mertens, Y T Lie, J Ongena, A Pospieszczyk, T Putz, J Rapp, D Rusbuld, R P Schorn, and B Schweer. The influence of impurities on limiter tokamak plasmas and relevant mechanisms. Plasma Physics and Controlled Fusion, 37(11A):A241–A253, nov 1995.
- [23] J Rapp, M Z Tokar, L Knen, H R Koslowski, G Bertschinger, M Brix, H Claassen, R Jaspers, A Krmer-Flecken, K Ohya, V Philipps, A Pospieszczyk, U Samm, T Tanabe, G Telesca, B Unterberg, and G Van Oost. Transport studies of high-Z elements in neon edge radiation cooled discharges in TEXTOR-94. Plasma Physics and Controlled Fusion, 39(10):1615–1634, oct 1997.
- [24] R Neu, R Dux, A Geier, A Kallenbach, R Pugno, V Rohde, D Bolshukhin, J C Fuchs, O Gehre, O Gruber, J Hobirk, M Kaufmann, K Krieger, M Laux, C Maggi, H Murmann, J Neuhauser, F Rytter, A C C Sips, A Stbler, J Stober, W Suttrop, H Zohm, and the ASDEX Upgrade Team. Impurity behaviour in the ASDEX Upgrade divertor tokamak with large area tungsten walls. Plasma Physics and Controlled Fusion, 44(6):811–826, may 2002.
- [25] N. Fedorczak, P. Monier-Garbet, T. Pütterich, S. Brezinsek, P. Devynck, R. Dumont, M. Goniche, E. Joffrin, E. Lerche, B. Lipschultz, E. de la Luna, G. Maddison, C. Maggi, G. Matthews, I. Nunes, F. Rimini, E.R. Solano, P. Tamain, M. Tsalas, and P. de Vries. Tungsten transport and sources control in JET ITER-like wall H-mode plasmas. Journal of Nuclear Materials, 463:85 – 90, 2015. PLASMA-SURFACE INTERACTIONS 21.
- [26] P. Helander. Bifurcated neoclassical particle transport. Physics of Plasmas, 5(11):3999–4004, 1998.
- [27] C Angioni and P Helander. Neoclassical transport of heavy impurities with poloidally asymmetric density distribution in tokamaks. Plasma Physics and Controlled Fusion, 56(12):124001, 2014.
- [28] E A Belli, J Candy, and C Angioni. Pfirsch-Schlüter neoclassical heavy impurity transport in a rotating plasma. Plasma Physics and Controlled Fusion, 56(12):124002, nov 2014.
- [29] Patrick Maget, Judith Frank, Timothée Nicolas, Olivier Agullo, Xavier Garbet, and Hinrich Lütjens. Natural poloidal asymmetry and neoclassical transport of impurities in tokamak plasmas. Plasma Physics and Controlled Fusion, 62(2):025001, nov 2020.
- [30] F. L. Hinton and S. K. Wong. Neoclassical ion transport in rotating axisymmetric plasmas. The Physics of Fluids, 28(10):3082–3098, 1985.
- [31] R. Bilato, T. Odstreil, F.J. Casson, C. Angioni, M. Brambilla, Ye.O. Kazakov, and E. Poli. The impact of the ion-cyclotron-resonance location on the poloidal asymmetries of impurity density in an ICRF-heated rotating plasma. Nuclear Fusion, 57(5):056020, mar 2017.
- [32] E A Belli and J Candy. Kinetic calculation of neoclassical transport including self-consistent electron and impurity dynamics. Plasma Physics and Controlled Fusion, 50(9):095010, jul 2008.
- [33] E A Belli and J Candy. An Eulerian method for the solution of the multi-species drift-kinetic equation. Plasma Physics and Controlled Fusion, 51(7):075018, jun 2009.
- [34] E A Belli and J Candy. Full linearized fokker-planck collisions in neoclassical transport simulations. Plasma Physics and Controlled Fusion, 54(1):015015, dec 2011.
- [35] T. Fülöp and P. Helander. Nonlinear neoclassical transport in a rotating impure plasma with large gradients. Physics of Plasmas, 6(8):3066–3075, 1999.
- [36] F. L. Hinton and Marshall N. Rosenbluth. Transport properties of a toroidal plasma at low to intermediate collision frequencies. The Physics of Fluids, 16(6):836–854, 1973.
- [37] J. Dominski, C. S. Chang, R. Hager, P. Helander, S. Ku, and E. S. Yoon. Study of updown poloidal density asymmetry of high- Z impurities with the new impurity version of XGCa. Journal of Plasma Physics, 85(5):905850510, 2019.
- [38] S. K. Wong and V. S. Chan. Self-consistent poloidal electric field and neoclassical angular momentum flux. Physics of Plasmas, 16(12):122507, 2009.
- [39] C.E. Kessel. Bootstrap current in a tokamak. Nucl. Fusion, 34(9):1221–1238, 1994.
- [40] W. A. Houlberg, K. C. Shaing, S. P. Hirshman, and M. C. Zarnstorff. Bootstrap current and neoclassical transport in tokamaks of arbitrary collisionality and aspect ratio. Physics of Plasmas, 4(9):3230–3242, 1997.

- [41] E A Belli, J Candy, O Meneghini, and T H Osborne. Limitations of bootstrap current models. Plasma Physics and Controlled Fusion, 56(4):045006, mar 2014.
- [42] C. Bourdelle, J.F. Artaud, V. Basiuk, M. Bécoulet, S. Brémond, J. Bucalossi, H. Bufferand, G. Ciraolo, L. Colas, Y. Corre, X. Courtois, J. Decker, L. Delpech, P. Devynck, G. Dif-Pradalier, R.P. Doerner, D. Douai, R. Dumont, A. Ekedahl, N. Fedorczak, C. Fenzi, M. Firdaouss, J. Garcia, P. Ghendrih, C. Gil, G. Giruzzi, M. Goniche, C. Grisolia, A. Grosman, D. Guilhem, R. Guirlet, J. Gunn, P. Hennequin, J. Hillairet, T. Hoang, F. Imbeaux, I. Ivanova-Stanik, E. Joffrin, A. Kallenbach, J. Linke, T. Loarer, P. Lotte, P. Maget, Y. Marandet, M.L. Mayoral, O. Meyer, M. Missirlian, P. Mollard, P. Monier-Garbet, P. Moreau, E. Nardon, B. Pégourié, Y. Peysson, R. Sabot, F. Saint-Laurent, M. Schneider, J.M. Travère, E. Tsitronis, S. Vartanian, L. Vermare, M. Yoshida, and R. Zagorski and. WEST physics basis. Nuclear Fusion, 55(6):063017, may 2015.
- [43] Naval Research Laboratory. NRL Plasma Formulary.
- [44] L C Ingesson, H Chen, P Helander, and M J Mantsinen. Comparison of basis functions in soft x-ray tomography and observation of poloidal asymmetries in impurity density. Plasma Physics and Controlled Fusion, 42(2):161–180, jan 2000.
- [45] M. Valisa, L. Carraro, I. Predebon, M.E. Puiatti, C. Angioni, I. Coffey, C. Giroud, L. Lauro Taroni, B. Alper, M. Baruzzo, P. Belo daSilva, P. Buratti, L. Garzotti, D. Van Eester, E. Lerche, P. Mantica, V. Naulin, T. Tala, and M. Tsallas and. Metal impurity transport control in JET H-mode plasmas with central ion cyclotron radiofrequency power injection. Nuclear Fusion, 51(3):033002, feb 2011.
- [46] D. Estève, Y. Sarazin, X. Garbet, V. Grandgirard, S. Breton, P. Donnel, Y. Asahi, C. Bourdelle, G. Dif-Pradalier, C. Ehrlacher, C. Emeriau, Ph. Ghendrih, C. Gillot, G. Latu, and C. Passeron. Self-consistent gyrokinetic modeling of neoclassical and turbulent impurity transport. Nuclear Fusion, 58(3):036013, 2018.
- [47] P Donnel, X Garbet, Y Sarazin, Y Asahi, F Wilczynski, E Caschera, G Dif-Pradalier, P Ghendrih, and C Gillot. Turbulent generation of poloidal asymmetries of the electric potential in a tokamak. Plasma Physics and Controlled Fusion, 61(1):014003, nov 2018.
- [48] P Donnel, X Garbet, Y Sarazin, V Grandgirard, N Bouzat, E Caschera, G Dif-Pradalier, P Ghendrih, C Gillot, G Latu, and C Passeron. Neoclassical impurity flux in presence of turbulent generated poloidal asymmetries and pressure anisotropy. Plasma Physics and Controlled Fusion, 61(4):044006, mar 2019.

Appendix A. Derivation

The derivation of the model follows closely the one without toroidal rotation described in [29]. We consider an axisymmetric equilibrium with a magnetic field expressed as $\mathbf{B} = F\nabla\varphi + \nabla\varphi \times \nabla\psi$ and $J^{-1} = \nabla\psi \cdot \nabla\theta \times \nabla\varphi$. The steady state momentum equation of a species 'a' of fluid velocity \mathbf{V}_a writes:

$$-\frac{m_a n_a \Omega^2}{2} \nabla R^2 = -\nabla p_a + n_a e_a (\mathbf{E} + \mathbf{V}_a \times \mathbf{B}) + \mathbf{R}_a \quad (\text{A.1})$$

where \mathbf{R}_a is the friction force, and the inertial term on the LHS has been simplified by considering a pure rigid toroidal rotation of angular frequency Ω . We neglect in this analysis the neoclassical viscous tensor, which means that the impurity is assumed to be in the Pfirsch-Schlüter regime. The scalar product of equation (A.1) with $R^2 \nabla\varphi$ gives the radial particle flux:

$$\Gamma_a \cdot \nabla\psi = -n_a \mathbf{E} \cdot R^2 \nabla\varphi - \frac{\mathbf{R}_a}{e_a} \cdot R^2 \nabla\varphi \quad (\text{A.2})$$

and using the relation :

$$R^2 \nabla \varphi = \frac{F}{B^2} \mathbf{B} - \frac{\mathbf{B} \times \nabla \psi}{B^2} \quad (\text{A.3})$$

we obtain:

$$\Gamma_a \cdot \nabla \psi = -n_a \frac{F}{B^2} \left(\mathbf{E} \cdot \mathbf{B} + \frac{\mathbf{R}_a \cdot \mathbf{B}}{e_a n_a} \right) + \frac{\mathbf{R}_a}{e_a} \cdot \frac{\mathbf{B} \times \nabla \psi}{B^2} + n_a \mathbf{E} \cdot \frac{\mathbf{B} \times \nabla \psi}{B^2} \quad (\text{A.4})$$

where we have, using $\mathbf{E} \equiv -\nabla \phi$ (we neglect $\partial_t \psi$):

$$\mathbf{E} \cdot \frac{\mathbf{B} \times \nabla \psi}{B^2} = -\frac{F}{JB^2} \partial_\theta \phi \quad (\text{A.5})$$

The projection parallel to \mathbf{B} of equation (A.1) gives, using $J \equiv 1/\mathbf{B} \cdot \nabla \theta$:

$$\mathbf{E} \cdot \mathbf{B} + \frac{\mathbf{R}_a \cdot \mathbf{B}}{e_a n_a} = \frac{1}{J} \left(\frac{\partial_\theta p_a}{e_a n_a} - \frac{m_a \Omega^2}{2e_a} \partial_\theta R^2 \right) \quad (\text{A.6})$$

which, injected into equation (A.4) gives:

$$\Gamma_a \cdot \nabla \psi = -\frac{F}{e_a JB^2} \left(\partial_\theta p_a + e_a n_a \partial_\theta \phi - \frac{m_a n_a \Omega^2}{2} \partial_\theta R^2 \right) + \frac{\mathbf{R}_a}{e_a} \cdot \frac{\mathbf{B} \times \nabla \psi}{B^2} \quad (\text{A.7})$$

The first term is the neoclassical flux and the second one is the classical flux.

Appendix A.1. Neoclassical flux

From equation (A.6) we get:

$$R_{a\parallel} = \frac{n_a T_a}{JB} \left[\frac{\partial_\theta p_a}{n_a T_a} + \frac{e_a}{T_a} \partial_\theta \phi - \frac{m_a \Omega^2}{2T_a} \partial_\theta R^2 \right] \quad (\text{A.8})$$

so that equation (A.7) becomes:

$$\Gamma_a^{neo} \cdot \nabla \psi = -\frac{F}{e_a B} R_{a\parallel} \quad (\text{A.9})$$

The parallel friction can be expressed as:

$$R_{a\parallel} = -n_a m_a \nu_a \left(V_{a\parallel} - V_{i\parallel} + C_0^a \frac{2q_{\parallel i}}{5p_i} \right) \quad (\text{A.10})$$

$$C_0^a = \frac{3}{2} \frac{1}{1 + \frac{T_a m_i}{T_i m_a}} \quad (\text{A.11})$$

The assumption of stationarity $\nabla \cdot (n_a \mathbf{V}_a) = 0$ gives

$$\frac{1}{J} \partial_\psi (J n_a \mathbf{V}_a \cdot \nabla \psi) + \frac{1}{J} \partial_\theta (J n_a \mathbf{V}_a \cdot \nabla \theta) + \frac{1}{J} \partial_\varphi (J n_a \mathbf{V}_a \cdot \nabla \varphi) = 0 \quad (\text{A.12})$$

We assume that the first term is negligible. This is justified whenever the radial component of the velocity is small compared with its poloidal component. In the axisymmetric case ($\partial_\varphi = 0$) we then have :

$$\frac{\mathbf{V}_a \cdot \nabla \theta}{\mathbf{B} \cdot \nabla \theta} = \frac{K_a(\psi)}{n_a} \quad (\text{A.13})$$

where $K_a(\psi)$ is an unknown function.

From equation (A.1), the fluid velocity can be expressed as:

$$\mathbf{V}_a = \frac{V_{a\parallel}}{B} \mathbf{B} + \frac{T_a}{e_a} A_a \frac{\mathbf{B} \times \nabla \psi}{B^2} + \frac{T_a}{e_a} A_a^\theta \frac{\mathbf{B} \times \nabla \theta}{B^2} \quad (\text{A.14})$$

where

$$A_a = \partial_\psi \ln p_a + (e_a/T_a) \partial_\psi \phi - m_a \Omega^2 / (2T_a) \partial_\psi R^2 \quad (\text{A.15})$$

$$A_a^\theta = \partial_\theta \ln p_a + (e_a/T_a) \partial_\theta \phi - m_a \Omega^2 / (2T_a) \partial_\theta R^2 \quad (\text{A.16})$$

From the expression of \mathbf{V}_a we obtain

$$\frac{\mathbf{V}_a \cdot \nabla \theta}{\mathbf{B} \cdot \nabla \theta} = \frac{V_{a\parallel}}{B} + \frac{F}{B^2} \frac{T_a}{e_a} A_a \quad (\text{A.17})$$

This gives using equation (A.13):

$$V_{a\parallel} = \frac{K_a(\psi)}{n_a} B - \frac{T_a}{e_a} A_a \frac{F}{B} \quad (\text{A.18})$$

Similarly for the main ion parallel heat flux, using $\nabla \cdot \mathbf{q}_i = 0$ and $q_{\perp,i} = \frac{5}{2} p_i \mathbf{V}_{\mathbf{T}i}^*$ with $\mathbf{V}_{\mathbf{T}i}^* = (\mathbf{B} \times \nabla T_i) / (e_i B^2)$, we can write:

$$q_{i\parallel} = L_i(\psi) B - \frac{5}{2} \frac{p_i}{e_i} \frac{F}{B} \partial_\psi T_i \quad (\text{A.19})$$

Using the notation $u_{2\parallel i} = 2q_{i\parallel} B / (5p_i)$ we can write

$$\begin{aligned} u_{2\parallel i} &= \frac{2L_i(\psi)}{5 \langle n_i \rangle} \frac{B^2}{T_i N} - F \frac{\partial_\psi T_i}{e_i} \\ &= \langle u_{2\parallel i} \rangle \frac{B^2/N}{\langle B^2/N \rangle} + \left(\frac{B^2/N}{\langle B^2/N \rangle} - 1 \right) F \frac{\partial_\psi T_i}{e_i} \end{aligned} \quad (\text{A.20})$$

with $N = n_i / \langle n_i \rangle$, and we define :

$$u(\psi) = \frac{K_i(\psi)}{\langle n_i \rangle} - \frac{C_0^a}{\langle B^2/N \rangle} \left(F \frac{\partial_\psi T_i}{e_i} + \langle u_{2\parallel i} \rangle \right) \quad (\text{A.21})$$

This gives

$$\frac{R_{a\parallel}}{n_a m_a \nu_a} = \frac{F}{B} \left(\frac{T_a}{e_a} A_a - \frac{T_i}{e_i} A_i + C_0^a \frac{\partial_\psi T_i}{e_i} \right) - \frac{K_a}{n_a} B + u(\psi) \frac{B}{N} \quad (\text{A.22})$$

At equilibrium, since the surface average cancels the operator $(\mathbf{B} \cdot \nabla)$, we have (assuming isothermal flux surfaces):

$$T_a \langle B \nabla_{\parallel} \ln n_a \rangle + e_a \langle B \nabla_{\parallel} \phi \rangle - \frac{m_a \Omega^2}{2} \langle B \nabla_{\parallel} R^2 \rangle = 0 \quad (\text{A.23})$$

so that $\langle B R_{a\parallel} / n_a \rangle = 0$, and using equation (A.10) we obtain:

$$K_a \left\langle \frac{B^2}{n_a} \right\rangle - K_i \left\langle \frac{B^2}{n_i} \right\rangle + C_0^a \langle u_{2\parallel i} \rangle - F \frac{T_a}{e_a} \langle A_a \rangle + F \frac{T_i}{e_i} \langle A_i \rangle = 0 \quad (\text{A.24})$$

This gives, using equations (A.21) and (A.24) to eliminate K_i and K_a :

$$\begin{aligned} \frac{R_{a\parallel}}{n_a m_a \nu_a} &= \frac{F}{B} \frac{T_a}{e_a} \left[\mathcal{G}_\psi \left(1 - \frac{b^2/n}{\langle b^2/n \rangle} \right) + \mathcal{U}_\psi \left\langle \frac{b^2}{N} \right\rangle \left(\frac{b^2/N}{\langle b^2/N \rangle} - \frac{b^2/n}{\langle b^2/n \rangle} \right) \right. \\ &\quad \left. + \frac{m_a \Omega^2}{2T_a} \left(1 - \frac{m_i}{m_a} \frac{e_a}{e_i} \right) \left(\frac{b^2/n}{\langle b^2/n \rangle} \langle \partial_\psi R^2 \rangle - \partial_\psi R^2 \right) \right] \end{aligned} \quad (\text{A.25})$$

with

$$\mathcal{G}_\psi \equiv \partial_\psi \ln p_a - \frac{T_i}{T_a} \frac{e_a}{e_i} \partial_\psi \ln p_i + C_0^a \frac{T_i}{T_a} \frac{e_a}{e_i} \partial_\psi \ln T_i \quad (\text{A.26})$$

$$\mathcal{U}_\psi \equiv u(\psi) \frac{\langle B^2 \rangle}{F} \frac{e_a}{T_a} \quad (\text{A.27})$$

The surface average neoclassical flux can then be derived from equation (A.9):

$$\begin{aligned} \langle \Gamma_a^{neo} \cdot \nabla \psi \rangle &= m_a \nu_a \langle n_a \rangle \frac{F^2 T_a}{e_a^2 \langle B^2 \rangle} \left[\left(\frac{1}{\langle b^2/n \rangle} - \left\langle \frac{n}{b^2} \right\rangle \right) \mathcal{G}_\psi + \left(\frac{\langle b^2/N \rangle}{\langle b^2/n \rangle} - \left\langle \frac{n}{N} \right\rangle \right) \mathcal{U}_\psi \right. \\ &\quad \left. + \frac{m_a \Omega^2}{2T_a} \left(1 - \frac{m_i}{m_a} \frac{e_a}{e_i} \right) \left(\left\langle \frac{n \partial_\psi R^2}{b^2} \right\rangle - \frac{\langle \partial_\psi R^2 \rangle}{\langle b^2/n \rangle} \right) \right] \end{aligned} \quad (\text{A.28})$$

Appendix A.2. Classical flux

The classical flux can be calculated from:

$$R_{a\perp} = -n_a m_a \nu_a (\mathbf{V}_{a\perp} - \mathbf{V}_{i\perp} + C_a^0 \mathbf{V}_{Ti}) \quad (\text{A.29})$$

This gives, using equation (A.14) in the simplified case where $\nabla \psi \cdot \nabla \theta \approx 0$:

$$\begin{aligned} \langle \Gamma_a^{cl} \cdot \nabla \psi \rangle &= - \frac{m_a \nu_a \langle n_a \rangle F^2 T_a}{e_a^2 \langle B^2 \rangle} \left[\left(\frac{\langle B^2 \rangle}{F^2} \langle n R^2 \rangle - \left\langle \frac{n}{b^2} \right\rangle \right) \mathcal{G}_\psi \right. \\ &\quad \left. - \frac{m_a \Omega^2}{2T_a} \left(1 - \frac{m_i}{m_a} \frac{e_a}{e_i} \right) \left(\frac{\langle B^2 \rangle}{F^2} \langle n R^2 \partial_\psi R^2 \rangle - \left\langle \frac{n \partial_\psi R^2}{b^2} \right\rangle \right) \right] \end{aligned} \quad (\text{A.30})$$

Appendix A.3. Poloidal asymmetry

The poloidal asymmetry can be obtained from equation (A.8) assuming isothermal flux surfaces:

$$\partial_\theta \ln n_a + \frac{e_a}{T_a} \partial_\theta \phi - \frac{m_a \Omega^2}{2T_a} \partial_\theta R^2 = JB \frac{R_{a\parallel}}{n_a T_a} \quad (\text{A.31})$$

where

$$\begin{aligned} JB \frac{R_{a\parallel}}{n_a T_a} &= \mathcal{A}_\psi \left\{ \left(1 - \frac{b^2/n}{\langle b^2/n \rangle} \right) \mathcal{G}_\psi + \left(\frac{b^2}{N} - \left\langle \frac{b^2}{N} \right\rangle \right) \frac{b^2/n}{\langle b^2/n \rangle} \mathcal{U}_\psi \right. \\ &\quad \left. + \frac{m_a \Omega^2}{2T_a} \left(1 - \frac{m_i}{m_a} \frac{e_a}{e_i} \right) \left(\frac{b^2/n}{\langle b^2/n \rangle} \langle \partial_\psi R^2 \rangle - \partial_\psi R^2 \right) \right\} \end{aligned} \quad (\text{A.32})$$

with $\mathcal{A}_\psi = JF m_a \nu_a / e_a$.

Appendix B. Large aspect ratio

In the large aspect ratio limit we have:

$$\partial_\psi r = q / (r B_0) \quad (\text{B.1})$$

The cos and sine components required for determining the poloidal asymmetry (equation A.32) are:

$$b^2/n = 1 - (2\epsilon + \delta) \cos \theta - \Delta \sin \theta \quad (\text{B.2})$$

$$n/b^2 = 1 + (2\epsilon + \delta) \cos \theta + \Delta \sin \theta \quad (\text{B.3})$$

$$\partial_r R^2 = r + 2R_0 \cos \theta \quad (\text{B.4})$$

with $\epsilon = r/R_0$. For the determination of the fluxes (equations A.28 and A.30), we use

$$R^2 \approx \frac{F^2}{B^2} \left[1 + \left(\frac{\epsilon}{q} \right)^2 \right] \quad (\text{B.5})$$

with $F \approx R_0 B_0$ to obtain

$$\langle n R^2 \rangle = \frac{R_0^2 B_0^2}{\langle B^2 \rangle} \left\langle \frac{n}{b^2} \right\rangle \left[1 + \left(\frac{\epsilon}{q} \right)^2 \right] \quad (\text{B.6})$$

$$\langle n R^2 \partial_r R^2 \rangle = \frac{R_0^2 B_0^2}{\langle B^2 \rangle} \left\langle \frac{n \partial_r R^2}{b^2} \right\rangle \left[1 + \left(\frac{\epsilon}{q} \right)^2 \right] \quad (\text{B.7})$$

We have also, following [27]:

$$\langle b^2/n \rangle = 1 + \epsilon \delta + \frac{\delta^2 + \Delta^2}{2} \quad (\text{B.8})$$

$$\langle n/b^2 \rangle = 1 + \epsilon \delta + 2\epsilon^2 \quad (\text{B.9})$$

This gives

$$\left\langle \frac{n}{b^2} \partial_r R^2 \right\rangle - \frac{\langle \partial_r R^2 \rangle}{\langle b^2/n \rangle} \approx 2\epsilon R_0 \left(1 + \frac{\delta}{2\epsilon} \right) \quad (\text{B.10})$$

$$\frac{\langle \partial_r R^2 \rangle}{\langle b^2/n \rangle} \frac{b^2}{n} - \partial_r R^2 \approx -R_0 (2 \cos \theta + \epsilon \Delta \sin \theta) \quad (\text{B.11})$$